Neuroinvasion and anosmia are independent phenomena upon infection with SARS-CoV-2 and its variants

Short title: Brain invasion by SARS-CoV-2

Guilherme Dias de Melo[1], Victoire Perraud[1§], Flavio Alvarez[2,3§], Alba Vieites-Prado[4§], Seonhee Kim[1], Lauriane Kergoat[1], Anthony Coleon[1], Bettina Salome Trüeb[5], Magali Tichit[6], Aurèle Piazza[7], Agnès Thierry[7], David Hardy[6], Nicolas Wolff[2], Sandie Munier[8], Romain Koszul[7], Etienne Simon-Lorière[9], Volker Thiel[10], Marc Lecuit[11,12], Pierre-Marie Lledo[13], Nicolas Renier[4], Florence Larrous[1#], Hervé Bourhy[1#*]

[1] Institut Pasteur, Université Paris Cité, Lyssavirus Epidemiology and Neuropathology Unit, F-75015 Paris, France

[2] Institut Pasteur, Université Paris Cité, Channel Receptors Unit, F-75015 Paris, France

[3] Sorbonne Université, Collège Doctoral, F-75005 Paris, France

[4] Institut du Cerveau et de la Moelle Épinière, Laboratoire de Plasticité Structurale, Sorbonne Université, INSERM U1127, CNRS UMR7225, 75013 Paris, France

[5] Institute of Virology and Immunology (IVI), Bern, Switzerland; Department of Infectious Diseases and Pathobiology, Vetsuisse Faculty, University of Bern, Bern, Switzerland

[6] Institut Pasteur, Université Paris Cité, Histopathology Platform, F-75015 Paris, France

[7] Institut Pasteur, Université Paris Cité, Spatial Regulation of Genomes Laboratory, F-75015 Paris, France

[8] Institut Pasteur, Université Paris Cité, Molecular Genetics of RNA viruses Unit, F-75015 Paris, France

[9] Institut Pasteur, Université Paris Cité, Evolutionary Genomics of RNA Viruses Group, F-75015 Paris, France

[10] Multidisciplinary Center for Infectious Diseases, University of Bern, Bern, Switzerland

[11] Institut Pasteur, Université Paris Cité, Inserm U1117, Biology of Infection Unit, 75015 Paris, France

[12] Necker-Enfants Malades University Hospital, Division of Infectious Diseases and Tropical Medicine, APHP, Institut Imagine, 75006, Paris, France

[13] Institut Pasteur, Université Paris Cité, Perception and Memory Unit, F-75015 Paris, France ; CNRS UMR3571, 75015 Paris, France

[§] these authors contributed equally
[#] senior author
[*] corresponding author: herve.bourhy@pasteur.fr

SUMMARY

Anosmia was identified as a hallmark of COVID-19 early in the pandemic, however, with the emergence of variants of concern, the clinical profile induced by SARS-CoV-2 infection has changed, with anosmia being less frequent. Here, we assessed the clinical, olfactory and neuroinflammatory conditions of golden hamsters infected with the original Wuhan SARS-CoV-2 strain, its isogenic ORF7-deletion mutant and three variants: Gamma, Delta, and Omicron/BA.1. We show that infected animals developed a variant-dependent clinical disease including anosmia, and that the ORF7 of SARS-CoV-2 contributes to the induction of olfactory dysfunction. Conversely, all SARS-CoV-2 variants were found to be neuroinvasive, regardless of the clinical presentation they induce. Taken together, this confirms that neuroinvasion and anosmia are independent phenomena upon SARS-CoV-2 infection. Using newly generated nanoluciferase-expressing SARS-CoV-2, we validated the olfactory pathway as a major entry point into the brain *in vivo* and demonstrated *in vitro* that SARS-CoV-2 travels retrogradely and anterogradely along axons in microfluidic neuron-epithelial networks.

Keywords: host-pathogen interaction, host adaptation, COVID-19, neurotropism, olfaction, olfactory bulbs, central nervous system, reverse genetics

Graphical asbtract

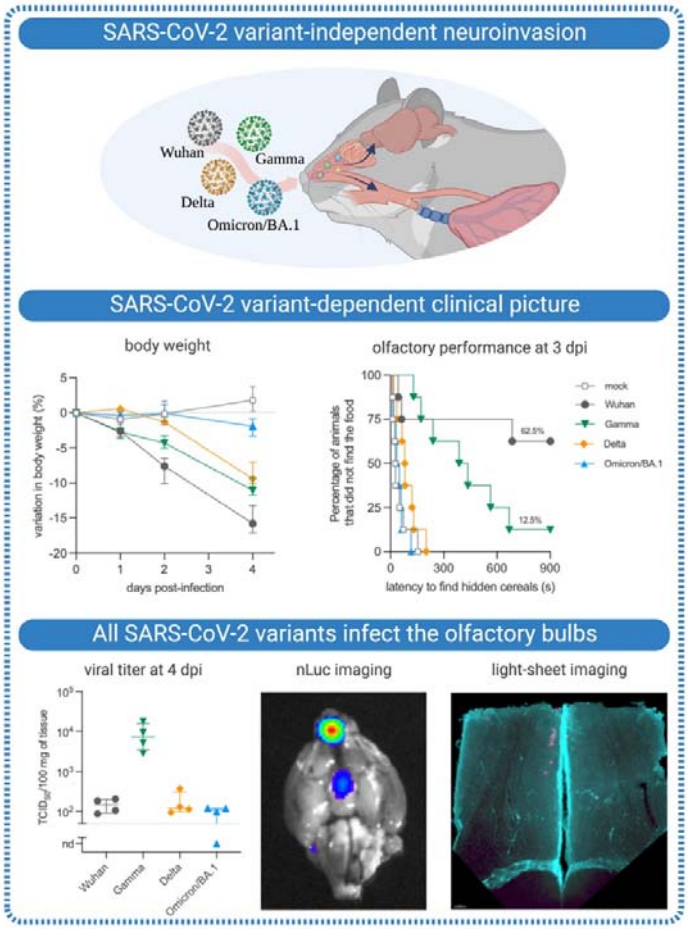

72 **INTRODUCTION**

73

74 The COVID-19 pandemic remains a major global public health problem. Since the beginning
75 of the pandemic in December 2019, more than 760 million cases have been confirmed, all SARS-
76 CoV-2 variants combined [1]. The original SARS-CoV-2 (Wuhan) gave rise to different variants of
77 concern (VoCs) in the first year of the pandemic (Alpha/B.1.1.7, Beta/B.1.351, Gamma/P.1), which
78 were almost totally replaced by the VoC Delta (B1.617.2, AY*) in 2020, by the VoC Omicron and its
79 lineages (e.g. BA.1, BA.2 and BA.5) in 2021-2022 and recombinants (XBB*) [1].

80 SARS-CoV-2 infects cells of the upper and lower airways, and COVID-19 manifests by a
81 multitude of respiratory and extra-respiratory symptoms, including neurological manifestations,
82 ranging from headache and dizziness to anosmia, ageusia and even stroke [2-4]. The neuropathology
83 of COVID-19 is currently considered to be a consequence of inflammation and hypoxia, rather than
84 direct viral invasion into the CNS [5,6]. However, with the emergence of the VoCs, and the increasing
85 rate of vaccination or previous infection, the symptomatology of COVID-19 has changed. In this
86 context, the clinical picture induced by the VoC Omicron/BA.1 is less severe or sometimes
87 asymptomatic, with a higher rate of upper airways involvement, sparing the olfactory mucosa and
88 consequently a lower incidence of anosmia, initially considered a hallmark of COVID-19 [7-13].

89 Previously, we determined that the infection of olfactory sensory neurons and loss of cilia
90 in the olfactory mucosa caused by SARS-CoV-2 Wuhan in humans and Syrian hamsters were
91 associated to olfaction loss, as well as to local inflammation and neuroinflammation in the olfactory
92 bulbs, attesting that the golden hamster is a relevant model to study the pathogenesis of SARS-
93 CoV-2 infection [14-16]. Other authors reported persistent microgliosis in the olfactory bulbs of
94 infected hamsters [17], and differences in the neuroinvasiveness and neurovirulence of VoCs have
95 been described [18]. Additionally, other authors have attempted to compare VoCs pathogenicity in
96 hamsters [19-21], but studies relating SARS-CoV-2 brain invasion to neurological symptoms are lacking.
97 In addition to the pathogenicity variation due to mutations in the spike of the variants, other viral
98 proteins may play a role in anosmia and local inflammation, including ORF7, which has been shown
99 to interfere with the host's innate immunity [22-24], with cell adhesion in the olfactory mucosa [25], and
100 with olfactory receptors [26].

101 Here, we identified that SARS-CoV-2 Wuhan and the VoCs Gamma, Delta and Omicron/BA.1
102 are all capable of invading the brain of Syrian hamsters and of eliciting a tissue-specific
103 inflammatory response. Using reverse genetics-generated bioluminescent viruses, we demonstrate
104 that SARS-CoV-2 infects the olfactory bulbs, but the clinical profile, including the olfactory
105 performance, is highly dependent on the variant. Further, deletion of the ORF7ab sequence in the
106 ancestral virus (Wuhan) reduces the incidence of olfaction loss without affecting the clinical picture

107 nor the neuroinvasiviness via the olfactory bulbs. Accordingly, this work validates that SARS-CoV-2
108 may travel inside axons and the olfactory pathway as the main entry route by SARS-CoV-2 into the
109 brain and corroborates the neurotropic potential of SARS-CoV-2 variants. Neuroinvasion and
110 anosmia are therefore independent phenomena upon SARS-CoV-2 infection.
111
112 **RESULTS**
113
114 **SARS-CoV-2 induces a clinical disease in hamsters, with a VoC-related severity difference**
115 We first investigated the differences in the clinical picture induced by different SARS-CoV-2
116 VoCs in comparison with the ancestral virus (Wuhan). We first tested the *in vitro* growth curves of
117 these viruses in Vero-E6 cells, and found no significant differences (Fig. S1A). Then, male golden
118 hamsters were inoculated intranasally with $6x10^4$ PFU of SARS-CoV-2 Wuhan, or the VoCs Gamma,
119 Delta or Omicron/BA.1 and followed them up for 4 days post-infection (dpi). All SARS-CoV-2-
120 infected animals presented a progressive loss of weight; however, a variant effect was observed
121 (Kruskal-Wallis P<0.0001, Fig. 1A-B), with SARS-CoV-2 Wuhan-infected animals presenting the most
122 intense median weight loss (15.8%, interquartile range 'IQR' 3.9%), followed by Gamma-infected
123 animals (11.0%, IQR 2.6%), Delta-infected animals (9.4%, IQR 3.1%) and Omicron/BA.1-infected
124 animals (1.9%, IQR 2.5%). Non-specific sickness-related clinical signs (ruffled fur, slow movement,
125 apathy) followed the same pattern (Kruskal-Wallis P<0.0001, Fig. 1D-E), with SARS-CoV-2 Wuhan-
126 infected animals presenting the worse clinical picture, followed by Gamma- and Delta-infected
127 animals, while Omicron/BA.1-infected animals presented a delayed manifestation of mild signs,
128 clinically observable at 4 dpi only.
129 Olfaction loss is a typical clinical sign of SARS-CoV-2 Wuhan-infected hamsters [14], however
130 olfactory deficit differed according to the different VoCs (Chi-square for trend P<0.0001): 62.5%
131 (5/8) of SARS-CoV-2 Wuhan-infected animals presented loss of olfaction (Log-rank test compared to
132 the mock P=0.0012), only 12.5% (1/8) of Gamma-infected animals lost olfaction completely with
133 62.5% (5/8) presenting an impaired olfactory performance (*i.e.* longer time to find the hidden
134 cereals) (Log-rank test compared to the mock P<0.0001). In contrast, none of the Delta- and
135 Omicron/BA.1-infected animals presented signs of olfactory impairment (Fig. 1G-H). All animals
136 found the visible food during the control test, demonstrating that no sickness behavior, visual
137 impairment, or locomotor deficit was responsible for the delay in finding the hidden food.
138 Several mutations on the spike distinguish the different VoCs. Furthermore, some VoC
139 isolates also present deletions in the ORF7 sequence [27-30], including the Delta isolate used in the
140 present study (deletion spanning positions 27506 to 27540 of the reference SARS-CoV-2 Wuhan
141 genome, which generates a stop codon; Fig. S1D). Since a possible link between ORF7b and

142 olfaction loss has been proposed [25], we constructed a recombinant SARS-CoV-2 based on the CoV-
143 2/W backbone, where the ORF7ab sequence was replaced by that of GFP (SARS-CoV-2
144 Wuhan/ΔORF7ab) (Fig. S4A). Remarkably, the clinical profile exhibited by Wuhan/Δ ORF7ab-
145 infected hamsters was similar to the one caused by the wild-type SARS-CoV-2 Wuhan (Fig. 1A-F),
146 showing that ORF7ab is not essential for viral infection and replication. However, the olfaction loss
147 incidence decreased significantly; only 25% (2/8) of the infected animals presented signs of
148 anosmia, in contrast to the 62.5% (5/8) observed in CoV-2/SARS-COV-2 Wuhan-infected hamsters
149 (Fig. 1G-H). Despite this reduction in anosmia incidence, Wuhan/ΔORF7ab was still detected in the
150 airways and in the olfactory bulbs of infected animals, with even higher titers (Fig. 2A-B).

151 Regarding lung pathology, as for the other clinical parameters, lung enlargement and lung
152 weight-to-body weight (LW/BW) ratio were significantly higher in SARS-COV-2 Wuhan- and in
153 Wuhan/ΔORF7ab-infected animals; Gamma- and Delta-infected animals presented intermediate
154 values, whereas Omicron/BA.1-infected animals' values were close to those of the ones of mock-
155 infected animals (Kruskal-Wallis $P<0.0001$, Fig. 1C and 1F). Likewise, the histopathological findings
156 in the lungs followed the same tendency: congestion, edema, mononuclear cells infiltration,
157 thickening of the alveolar walls and bronchiolar epithelium desquamation were observed in all
158 infected animals (Fig. S2A), along with a diffuse SARS-CoV-2 nucleocapsid staining (Fig. S2B), with
159 more severe alterations observed in the lungs of SARS-COV-2 Wuhan-infected animals than in
160 Gamma-, Delta-, and Omicron/BA.1-infected hamsters.

161 In a multivariate analysis of clinical parameters recorded at 4 dpi, the two-first principal
162 components explained 91.9% of sample variability. Body weight loaded negatively to PC1 (principal
163 component) and negatively correlated with the clinical score and the LW/BW ratio, whereas the
164 olfactory performance loaded positively to PC2 (Fig. S3A). In the principal component analysis (PCA)
165 plot regarding tissue-related inflammation, the difference among groups was marked: mock and
166 Omicron/BA.1-infected animals loaded homogeneously and relatively close, followed by the Delta-
167 infected animals. SARS-COV-2 Wuhan-, Wuhan/ΔORF7ab-, and Gamma-infected animals loaded in
168 a more dispersed way, far away from the other VoCs, effect of the olfactory performance deficit
169 and clinical severity (Fig. S3C).

170

171 **SARS-CoV-2-infected airways respond to the infection regardless of the viral variants**

172 Next, we measured the viral titer and RNA loads in the upper airways (nasal turbinates),
173 and in the lower airways (lung). Infectious viruses were detected in the nasal turbinates and in the
174 lungs of all infected hamsters regardless of the VoC, however, a variant effect was observed, with
175 the highest values for the Gamma-infected animals, and the lowest values for the Omicron/BA.1-

176 infected animals (Kruskal-Wallis P<0.0001, Fig. 2A). Genomic and sub-genomic SARS-CoV-2 RNA
177 were detected equally in the lungs of all infected animals; but differently in the nasal turbinates,
178 regardless of the positivity of all samples, Delta-infected animals presented the highest viral load
179 (Kruskal-Wallis P=0.0023, Fig. 2B).

180 Both the upper and lower airways responded to the infection by all VoCs (Fig. 2CD), but
181 with a tissue-specific inflammatory signature: in the lungs, *Mx2, Il-6, Cxcl10* and *Il-10* were
182 upregulated for all VoCs, and the highest in SARS-COV-2 Wuhan-infected animals (Fig. 2C). In the
183 nasal turbinates, the gene expression of *Ifn-β* and *Il-6* presented the highest values in SARS-COV-2
184 Wuhan-infected animals and the lowest in Omicron/BA.1-infected animals. *Mx2*, *Cxcl10* and *Il-10*
185 expression were the highest in Delta-infected animals while Omicron/BA.1-infected animals
186 showed the lowest levels (Fig. 2D). Interestingly, Wuhan/ΔORF7ab infection induced a different
187 lung inflammatory signature compared to Wuhan or the other VoCs, represented by a higher
188 expression of *Mx2* and *Ifn-β* (Fig. 2C). In the nasal turbinates, Wuhan/ΔORF7ab infection also
189 induced a higher expression of *Mx2,* but also *Il-6*, *Cxcl10, Tnf-α* and *Il-10* (Fig. 2D). To better
190 appreciate the tissue- *vs.* virus-related gene expression, we performed a multivariate analysis of
191 these data. Interestingly, the two-first principal components explained 79.5% of sample variability
192 (Fig. S3B). In the PCA plots, the nasal turbinates of all infected hamsters were loaded in proximity to
193 each other (Fig. S3D), whereas the lungs were separated by an important effect of *Il-6, Cxcl10* and
194 *Il-10* (Fig. S3D).

195

196 **SARS-CoV-2 neuroinvasion and neuroinflammation in the olfactory bulbs**

197 After establishing the clinical and inflammatory profile of the infected animals, we aimed to
198 assess the effect of infection on the olfactory bulbs. Remarkably, even if the olfactory performance
199 differed according to the VoCs (Fig. 1G-H), positive viral titers were detected in the olfactory bulbs
200 of animals from all infected groups, with Wuhan/ΔORF7ab and Gamma-infected animals presenting
201 the highest titer at 4 dpi (Kruskal-Wallis P=0.0096, Fig. 2A). These findings were corroborated by
202 the detection of genomic viral RNA in the olfactory bulbs of animals from all infected groups as
203 well, but viral RNA load was higher in SARS-COV-2 Wuhan-infected animals (Kruskal-Wallis
204 P=0.0104, Fig. 2B). Conversely, in these samples, the sub-genomic RNA was below the detection
205 limit.

206 The olfactory bulbs presented an intrintriguing inflammatory profile. The antiviral *Mx2*
207 gene, along with the inflammatory genes *Ifn-β*, *Il-6* and *Cxcl10* were highly upregulated in the
208 olfactory bulbs of all infected hamsters (Fig. 2E), regardless of their olfactory performance in the
209 food-finding test (Fig. 1 G-H), yet *Il-10* expression was highly upregulated in the olfactory bulbs of

210 SARS-COV-2 Wuhan/ΔORF7ab-infected animals (compared to the mock). Unexpectedly, the gene
211 expression of these selected targets tended to be higher in the olfactory bulbs of Delta-infected
212 animals (Fig. 2E). In a multivariate analysis for tissue- and virus-related gene expression, the
213 olfactory bulbs from SARS-COV-2 Wuhan-infected animals tended to load in proximity to the
214 corresponding nasal turbinates (effect of *Il-6*, *Cxcl10* and *Il-10*), whereas olfactory bulbs from
215 Gamma-, Delta- and Omicron/BA.1-infected animals loaded separately, possibly reflecting the
216 impact of *Mx2*, *Tnf-*α and *Ifn-*β differential expression (Fig. S3D).

217 Having detected the virus in the olfactory bulbs using virologic and molecular techniques,
218 we aimed to visualize the infection. We examined the SARS-CoV-2 Wuhan distribution in the whole
219 brain by combining whole-head tissue clearing with light sheet microscopy imaging using iDISCO+
220 [31]. At 4 dpi, all Wuhan-infected hamsters displayed a diffuse viral distribution in the nasal cavity:
221 nasal turbinates and olfactory epithelium (Fig. 3A and Video S1). Along the same lines, all SARS-
222 COV-2 Wuhan-infected animals presented SARS-CoV-2 in the olfactory bulbs in sparse neurons,
223 localized in the proximity of the olfactory nerve entry point (Fig. 3B and Video S1). Using this
224 technique, no infected cells were observed in other areas of the brain and no alteration in the
225 vascular network was detected.

226 We next used a complementary method to visualize the infection of the olfactory bulbs. To
227 this end, we generated recombinant viruses that express the nanoluciferase by reverse genetics
228 (Wuhan_nLuc, Wuhan/ΔORF7ab_nLuc, and Delta_nLuc; Fig. S1B-C and S4A). The disease profile
229 induced by these three novel recombinant viruses was similar to the profile induced by the wild-
230 type parental viruses (Fig. 3C). *In vivo* imaging of infected hamsters was performed at 4 dpi using
231 fluorofurimazine (FFz) as substrate. Very low positive signals were observed in the nasal cavity
232 region, possibly due to the thickness of the skin and bones that could block the light emission, but
233 significantly higher in the Wuhan_nLuc than in the Wuhan/ΔORF7ab_nLuc the Delta_nLuc (Kruskal-
234 Wallis P=0.0107, Fig. S4BC). More sensitive results were obtained during the *ex vivo* imaging. After
235 euthanasia, the lungs and brains were collected and imaged. Positive signals in the lungs were
236 obtained at the same intensity for the three viruses (Fig. 3D), and presented a multi-focal/diffuse
237 distribution (Fig. 3E and S4D). The brains were imaged in the ventral position in order to better
238 expose the olfactory bulbs. Intense luminescent signals were recorded from the brains of hamsters
239 infected with all viruses; when placing the ROI (region of interest) exclusively in the olfactory bulbs,
240 intensity was higher in Wuhan_nLuc compared to Delta_nLuc; conversely, when considering the
241 whole brain ventral area, intensity was higher in Delta_nLuc. Wuhan/ΔORF7ab_nLuc induced
242 intermediate values (Fig. 3C and S4D), which might reflect the higher replication rate detected in
243 the olfactory bulbs infected Wuhan (Fig. 2B). Despite intensity differences, the olfactory bulbs were

244 the major infected structure in the brain, and sagittal views of the brain indicate that the origin of
245 the luminescent signal is the ventral part of the olfactory bulbs, which is situated above the
246 olfactory epithelium in the nasal cavity (Fig. 3E and S4E).
247
248 **Anosmia is not associated with viral load or infection of the olfactory bulbs**
249 All tested SARS-CoV-2 variants were found to be able to invade the CNS and infect the
250 olfactory bulbs, but the incidence of olfactory dysfunctions varied according to the VoC, with
251 hamsters infected with Delta and Omicron/BA.1 presenting no signs of anosmia (Fig. 1G-H). To test
252 if the viral inoculum could influence the neuroinvasiveness of SARS-CoV-2 and the incidence of
253 olfactory dysfunctions, we infected hamsters with a 2-log lower infectious dose of Wuhan ($6x10^2$
254 PFU). These animals were subjected to the same clinical-behavioral tests described above. In the
255 acute phase of the infection, up to 4 dpi, the low infectious dose induced similar body weight loss
256 and clinical score as the animals infected with the initial inoculum, as well as infectious viral titers in
257 the airways and in the olfactory bulbs (Fig. S5). Surprisingly, despite the presence of infectious virus
258 in the olfactory bulbs, animals infected with a lower infectious dose presented a lower incidence of
259 olfactory dysfunction (25%, 2/8).
260
261 **SARS-CoV-2 travels retrogradely and anterogradely along axons**
262 *In vitro*, monocultures of neurons are hardly infectable by SARS-CoV-2 and co-culture with
263 permissive cells is necessary [32]. Consequently, we developed a co-culture system with hNSC-derived
264 neurons and SARS-CoV-2-receptive epithelial cells (A549-hACE2-TMPRSS2 cells). We grew these co-
265 cultures using axonal diodes in microfluidic devices [33] to assess the ability of SARS-CoV-2 to infect
266 neurons and to move inside axons. In these devices, the co-cultures form neuron-epithelial
267 networks in both the left and the right chambers of the device (Fig. 4A-B), that are connected
268 exclusively via an unidirectional growth of axons from the left towards the right chamber (Fig. 4C).
269 Then, the right or the left chamber of the microfluidic devices was infected with the ancestral virus
270 (Wuhan), the Wuhan/ΔORF7ab and the VoCs Gamma, Delta and Omicron/BA.1. At 3 dpi, infected
271 cells were detected in both the right and the left chambers of all devices, attesting that the virus
272 travelled from the right to the left chamber inside the axons (retrograde axonal transport; Fig. 4D-H
273 and S6), and from the left to the right chamber inside the axons (anterograde axonal transport; Fig.
274 4I-M and S7). To further confirm the involvement of the axonal transportation of SARS-CoV-2, we
275 used ciliobrevin D, an inhibitor of the cytoplasmic dynein transport machinery which acts on the
276 bidirectional transport of organelles along axons [34]. When the infection occurred in the presence of
277 ciliobrevin D, the retrograde transport was blocked, and no SARS-CoV-2-infected cell was observed
278 in the left chamber (Fig. S8). To quantify the arrival of viral particles via the axons, we infected

microfluidic devices in both retrograde and anterograde conditions with the recombinant viruses expressing nanoluciferase Wuhan_nLuc, Wuhan/ΔORF7ab_nLuc, and Delta_nLuc, and we measured the luminescence in the supernatants on a daily basis (Figure S9). Positive nLuc activity was detected in the supernatants of all receiving chambers from 1 dpi, increasing progressively overtime (Figure S9G and S9H), indicative of retrograde and anterograde SARS-CoV-2 movement. The luminescence values in the infected chambers were constant and at the maximum limit of detection (Fig. S1).

DISCUSSION AND CONCLUSIONS

The neurotropism of SARS-CoV-2 is still a matter of debate [35]. While studies on natural infection in humans and experimental infection in animal models reported brain infection by SARS-CoV-2 [14,36-40], including in *in vitro* human models of infection [41-43], others failed to detect SARS-CoV-2 in the nervous tissue [5,44]. This inconsistency may be due to the time of infection, as in most cases the available samples are post-mortal, and we have demonstrated, in the hamster model, that viral isolation is time-dependent, with higher viral loads found in acute time-points[14]. Despite this open question, the impact of SARS-CoV-2 infection on the brain is undeniable [2,45-47]. Most of these published data is related to the original SARS-CoV-2 (Wuhan), however, less information concerning VoCs neuropathogenesis is available [10]. Here we show that all evaluated SARS-CoV-2 viruses (Wuhan, Gamma, Delta and Omicron/BA.1), including novel generated recombinant SARS-CoV-2, are able to invade the brain, most likely via the olfactory nerves, and of promoting inflammation in the nervous tissue.

Despite this shared neuroinvasiveness via the olfactory bulbs, disease profile and airways responses are quite dependent on the SARS-CoV-2 variant. Indeed, we show that all VoCs can infect golden hamsters and promote lung inflammation, including Omicron/BA.1 differently from other reports [19,48], probably due to infectious doses or viral isolates. A “variant-effect” in the clinical presentation and in the tissue-related inflammation was evident, with disease severity presenting the following order: SARS-CoV-2 Wuhan > Gamma > Delta > OmicronBA.1, which supports the hypothesis that Omicron/BA.1 evolution has resulted in a tropism more restricted to the upper respiratory tract, thereby causing a less severe clinical disease [10,49-51]. Although with different severities, neuroinvasiveness, neurotropism and neurovirulence [35] seem to be conserved features among SARS-CoV-2 variants. Indeed, the data presented herein give support to the neuroinvasive ability of SARS-CoV-2, as besides detection of viral RNA and isolation of infectious virus from the olfactory bulbs, we could clearly observe SARS-CoV-2 infected neurons in the brain of hamsters by

314 light sheet microscopy. Nevertheless in hamsters, unlike what has been reported in K18-hACE2
315 mice which ACE2 expression pattern is non-physiological and ectopic [37], detection of SARS-CoV-2-
316 infected cells was restricted to the olfactory bulbs, without evidence of brain vasculature
317 remodeling nor virus associated with blood vessels.

318 Olfactory bulb infection is therefore a common feature in the SARS-CoV-2 infectious
319 process, regardless of the variant considered. An inflammation response was also observed in this
320 tissue, with a common upregulation of the antiviral gene *Mx2*, regardless of the VoC. The reason
321 why some VoCs do not cause olfaction loss is still an open question. The infection and inflammation
322 of the olfactory bulbs, if involved in SARS-CoV-2-associated anosmia, does not seem to be enough
323 to cause olfaction loss in the golden hamster. Aggressions to the olfactory mucosa, rather than the
324 olfactory bulb, are indeed likely the main factors contributing to anosmia, as recovery from
325 anosmia has been related to regeneration of the olfactory epithelium in hamsters [52,53]. Moreover,
326 significant changes in the olfactory epithelium, such as apoptosis, architectural damages,
327 inflammation, downregulation of odorant receptors and functional changes in olfactory sensory
328 neurons, might also contribute, on top of the infection *per se*, to the occurrence of anosmia [10,14,54-
329 57]. Therefore, it seems that infection and inflammation combined are needed to trigger anosmia,
330 and the lower incidende of anosmia observed after infection by some VoCs is therefore linked to
331 lower levels of inflammation.

332 Furthermore, besides mutations in the spike sequence in the SARS-CoV-2 variants genome,
333 additional mutations may be present in other regions of the viral genome, including deletions in the
334 ORF7a and ORF7b sequences [27-30]. ORF7a and ORF7b have been related to viral-induced apoptosis,
335 and to interference with the innate immunity and the antiviral response [22-24,58,59], without, however,
336 being essential to viral infection and replication [60,61]. Further, ORF7b has the potential to interfere
337 with cell adhesion proteins in the olfactory mucosa [25], and interestingly, a binary interaction
338 between ORF7b and the human olfactory receptor OR1D5 has also been reported [26]. Deletions or
339 mutations in these regions may therefore play an additional role in the induction of olfactory
340 disturbances, by preserving the architecture and structures of the olfactory epithelium. Another
341 important point is that we can observe a similar clinical profile and low incidence of olfactory
342 disturbances as SARS-CoV-2 Wuhan/ΔORF7ab by simply reducing the viral inoculum of SARS-CoV-2
343 Wuhan. Regardless of a comparative evolution of body weight loss and clinical score [62], anosmia
344 was less frequent in animals infected with a low dose of SARS-CoV-2 Wuhan. This might be related
345 to the less severe initial aggression suffered by the olfactory epithelium due to lower infectious
346 doses [53,63] and may also explain why other studies did not detect olfaction dysfunction despite
347 detecting inflammatory changes in the brain [64].

348 Despite the occurrence or not of anosmia, SARS-CoV-2 can infect olfactory sensory neurons
349 and the olfactory bulb [10,14], and we show herein that the virus can infect neurons and travel inside
350 the axons in both retrograde and anterograde directions. SARS-CoV-2 neuroinvasion was
351 hypothesized to occur by axonal transport via cranial nerves (olfactory, vagus, trigeminal) or by the
352 hematogeneous route [35,65,66]. The data presented herein do not support hematogenous diffusion of
353 SARS-CoV-2 towards the brain, but corroborate the hypothesis of the olfactory pathway as a
354 preferential portal of entry towards the olfactory bulbs [67]. Brain infection via the olfactory pathway
355 therefore seems a common feature of coronaviruses [68,69], regardless of clinical disease
356 presentations. Finally, this study highlights that neuroinvasion and anosmia are therefore
357 independent phenomena upon SARS-CoV-2 infection.

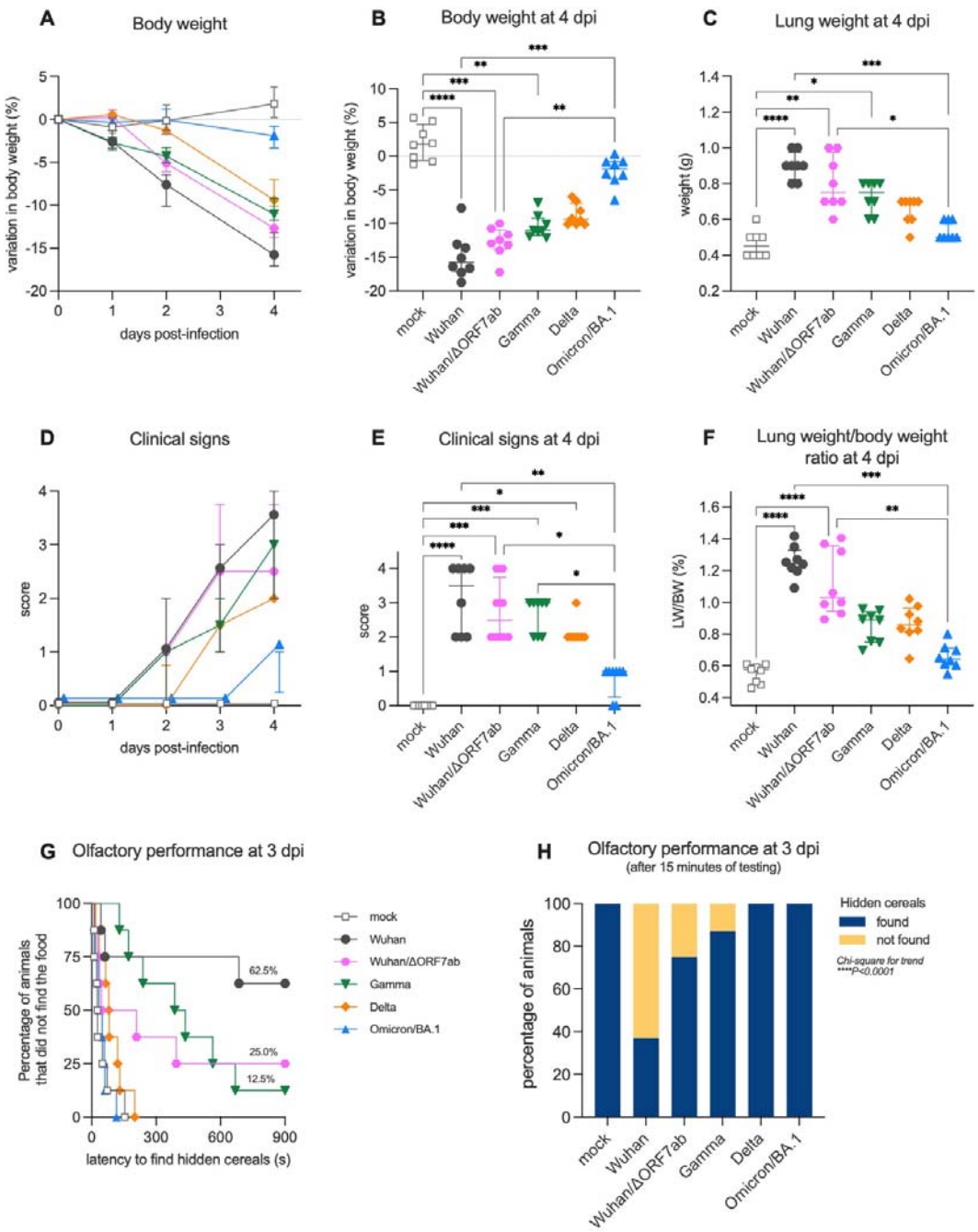

Figure 1. Clinical profile of hamsters infected with SARS-CoV-2 original virus (Wuhan), the recombinant Wuhan/ΔORF7ab or the variants of concern (VoC) Gamma, Delta, and Omicron/BA.1. AB. Body weight variation over four days post-infection. **C**. Lung weight measured at 4 dpi. **DE**. Clinical score over four days post-infection. The clinical score is based on a cumulative 0–4 scale: ruffled fur; slow movements; apathy; and absence of exploration activity. **F**. Lung weight-to-body weight ratio measured at 4 dpi. Horizontal lines indicate median and the interquartile range (n=8/group). Kruskal-Wallis test followed by the Dunn's multiple comparisons test (*P<0.05, **P<0.01, ***P<0.001, ****P<0.0001). **GH**. Olfactory performance measured at 3 days post-infection (dpi). The olfaction test is based on the hidden (buried) food finding test. Curves represent the olfactory performance of animals during the test (G) and bars represent the final results (H) (n=8/group). Chi-square test for trend (****P<0.0001). See Supplementary Figures 1 and 2.

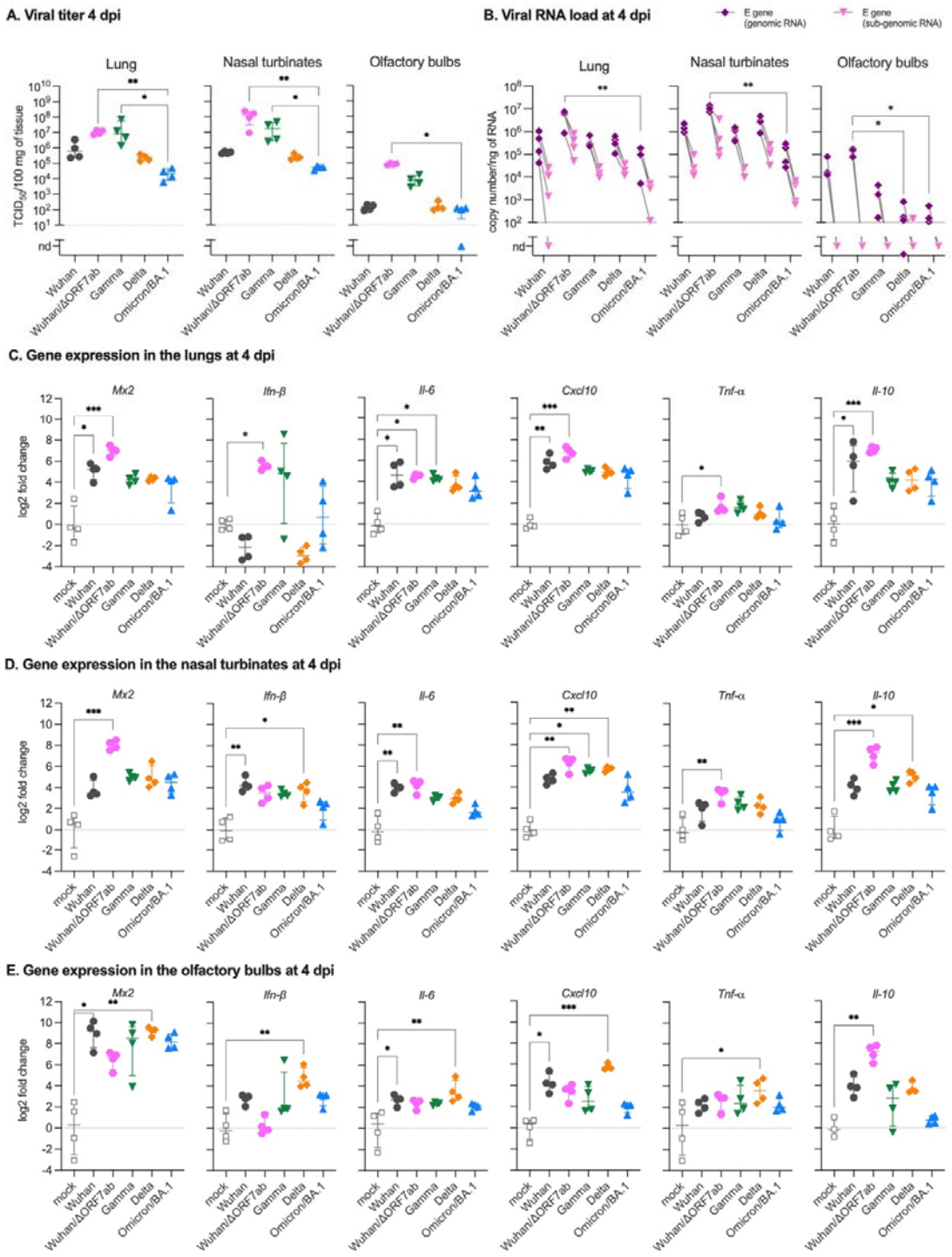

Figure 2. Virologic assessment and gene expression of selected immune mediators in different tissues of hamsters infected with SARS-CoV-2 original virus (Wuhan), the recombinant Wuhan/ΔORF7ab or the variants of concern (VoC) Gamma, Delta, and Omicron/BA.1. A. Infectious viral titers in the lung, nasal turbinates, and olfactory bulbs at 4 days post-infection (dpi) expressed as $TCID_{50}$ per 100 mg of tissue. Horizontal lines indicate median and the interquartile range (n=4/group). **B.** SARS-CoV-2 viral RNA load detected in the lung, nasal turbinates, and olfactory bulbs at 4 dpi. Genomic and sub-genomic viral RNA were assessed based on the E gene sequence. Horizontal lines indicate median and the interquartile range. Gray lines connect symbols

379 from the same animals (n=4/group). **C-E.** Gene expression values in the lung (C), nasal turbinates
380 (D) and olfactory bulbs (E) of *Mx2, Ifn*-β*, Il-6, Cxcl10, Tnf*-α and *Il-10* at 4 dpi. Horizontal lines
381 indicate median and the interquartile range (n=4/group). Kruskal-Wallis test followed by the Dunn's
382 multiple comparisons test (*P<0.05, **P<0.01). nd: not detected. See Supplementary Figures 1 and
383 2.
384

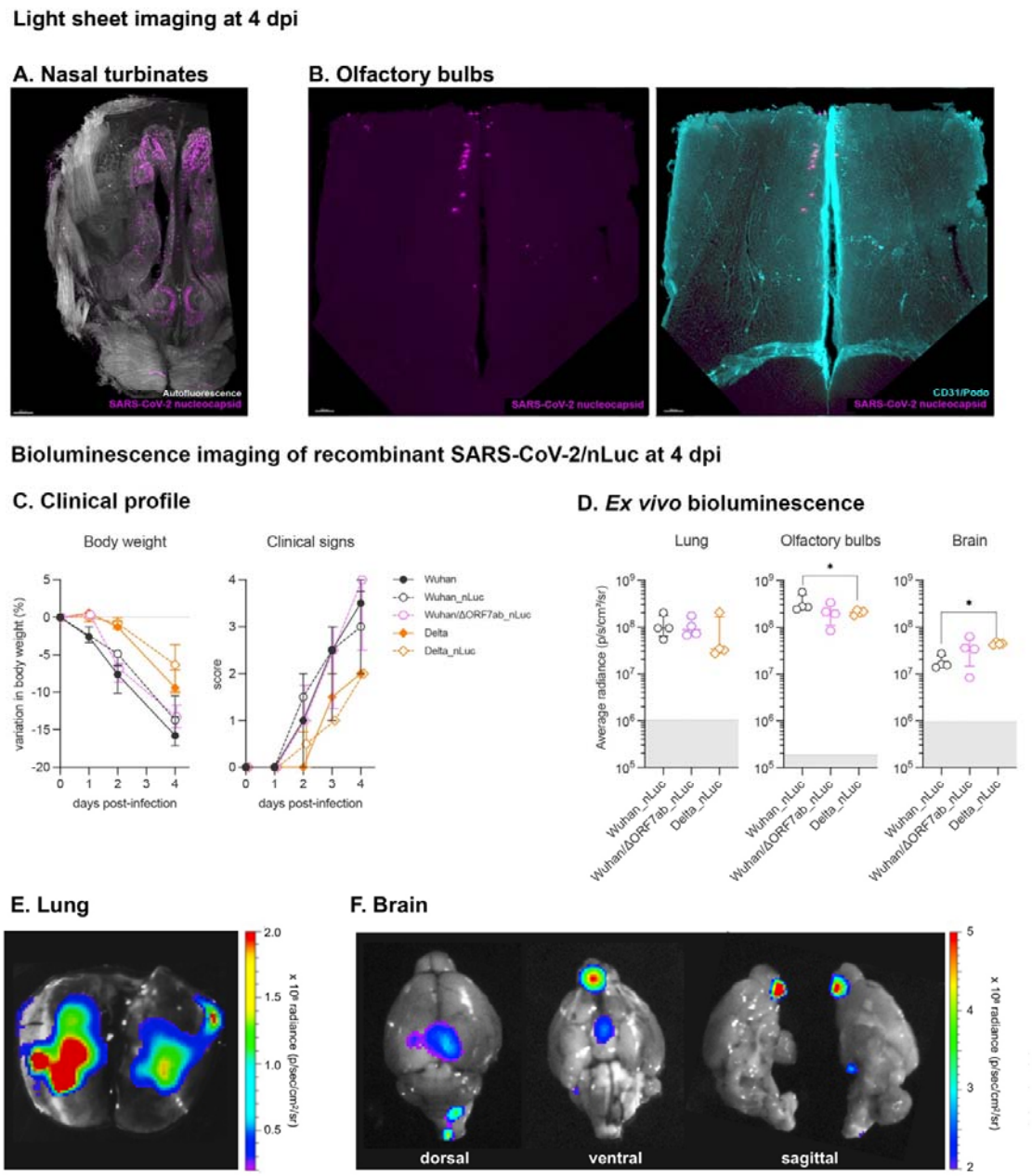

Figure 3. Imaging assessment of SARS-CoV-2 neuroinvasion. AB. iDISCO+ whole head clearing and immunolabeling against the SARS-CoV-2 nucleocapsid in hamsters infected with the SARS-CoV-2 original virus (Wuhan) at 4 days post-infection (dpi). **A.** Representative nasal turbinate (sagittal section from the skull) showing a diffuse distribution of SARS-CoV-2 (scale bar = 500 µm). **B.** Representative olfactory bulb section stained for SARS-CoV-2 nucleocapsid and for podoplanin (CD31/Podo) to identify the vascular compartment. Note presence of SARS-CoV-2 in olfactory bulb neurons, with no macroscopic alterations in the vascular network of the olfactory bulb. Scale bar: 200 µm. See supplementary video 1. **CF.** Bioluminescent recombinant SARS-CoV-2 viruses induce a clinical disease with infection of the olfactory bulbs. **C.** Clinical profile of hamsters infected with the recombinant viruses SARS-CoV-2 Wuhan_nLuc and Wuhan/ΔORF7ab_nLuc (based on the original SARS-CoV-2 Wuhan) and Delta_nLuc (based on the Delta variant). The body weight loss and the clinical score are comparable with those induced by wild-type viruses (n=4/group) (See Figure 1A). The clinical score is based on a cumulative 0–4 scale: ruffled fur; slow movements; apathy; and absence of exploration activity (See Figure 1D). **D.** *Ex vivo* bioluminescence values from the lungs,

400 the olfactory bulbs (ventral view), the brains (ventral view) at 4 dpi (n=4/group). Horizontal lines
401 indicate median and the interquartile range. Kruskal-Wallis test followed by the Dunn's multiple
402 comparisons test (*P<0.05). The gray crosshatched area corresponds to background signals
403 obtained from the same tissues of a mock-infected hamster. **EF.** Representative *ex vivo* imaging of a
404 lung (C) and a brain (D) of a hamster infected with a recombinant SARS-CoV-2 expressing the nLuc
405 at 4 dpi. Note that in the brain, the major bioluminescent focus is localized in the ventral face of
406 olfactory bulbs. See Supplementary Figure 3.
407
408
409

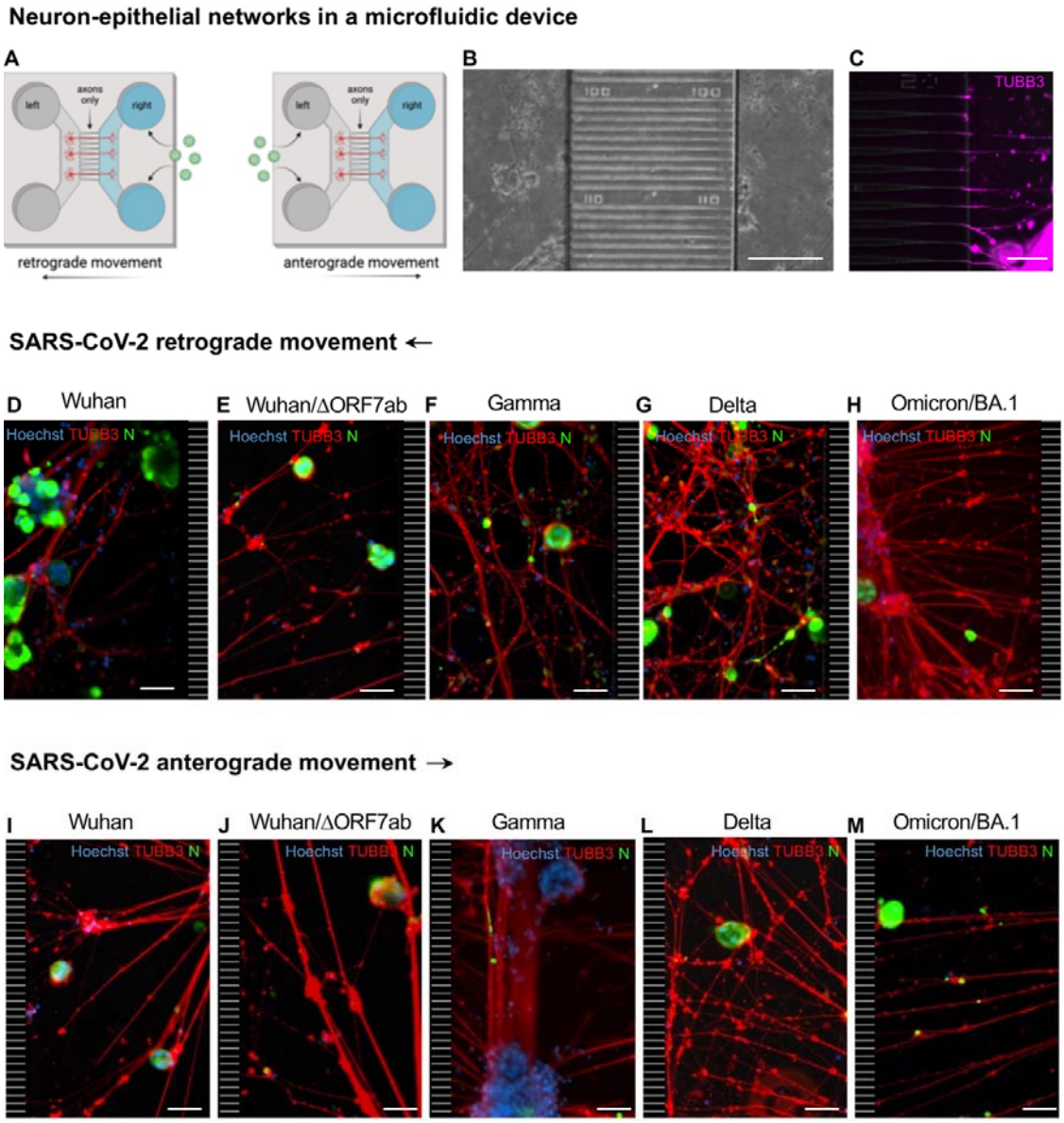

Figure 4. SARS-CoV-2 travels inside axons in *in vitro* neuron-epithelial networks. A. Schematic view of an axon diode in a microfluidic device where the left and the right chambers are connected exclusively by axons. In this study, SARS-CoV-2 was added in the right chamber (to assess the retrograde axonal transport) or in the left chamber (to assess the anterograde axonal transport). **B.** Bright field view of a neuron-epithelial network showing neuronal and A549-ACE2-TMPRSS2 co-culture in both chambers, separated by funnel-shaped micro-channels (scale bar = 200 µm). **C.** Detail of β-Tubulin III-positive axons crossing the funnel-shaped micro-channels and entering in the right chamber (scale bar = 50 µm). **D-H.** Neuron-epithelial networks infected at the right chamber with SARS-CoV-2 Wuhan (D), Wuhan/ΔORF7ab (E), Gamma (F), Delta (G) and Omicron/BA.1 (H) showing infected cells in the left chambers (scale bar = 50 µm). **I-M.** Neuron-epithelial networks infected at the left chamber with SARS-CoV-2 Wuhan (I), Wuhan/ΔORF7ab (J), Gamma (K), Delta (L), and Omicron/BA.1 (M) showing infected cells in the right chambers (scale bar = 50 µm). Hoechst: nuclei (blue). TUBB3: β-Tubulin III (red). N: SARS-CoV-2 nucleocapsid (green). The black and white striped zones in the right (D-H) and in the left (I-M) of the photomicrographs represents the microchannels, which are not accessible during immunostainings. See Supplementary Figures 6-9.

427

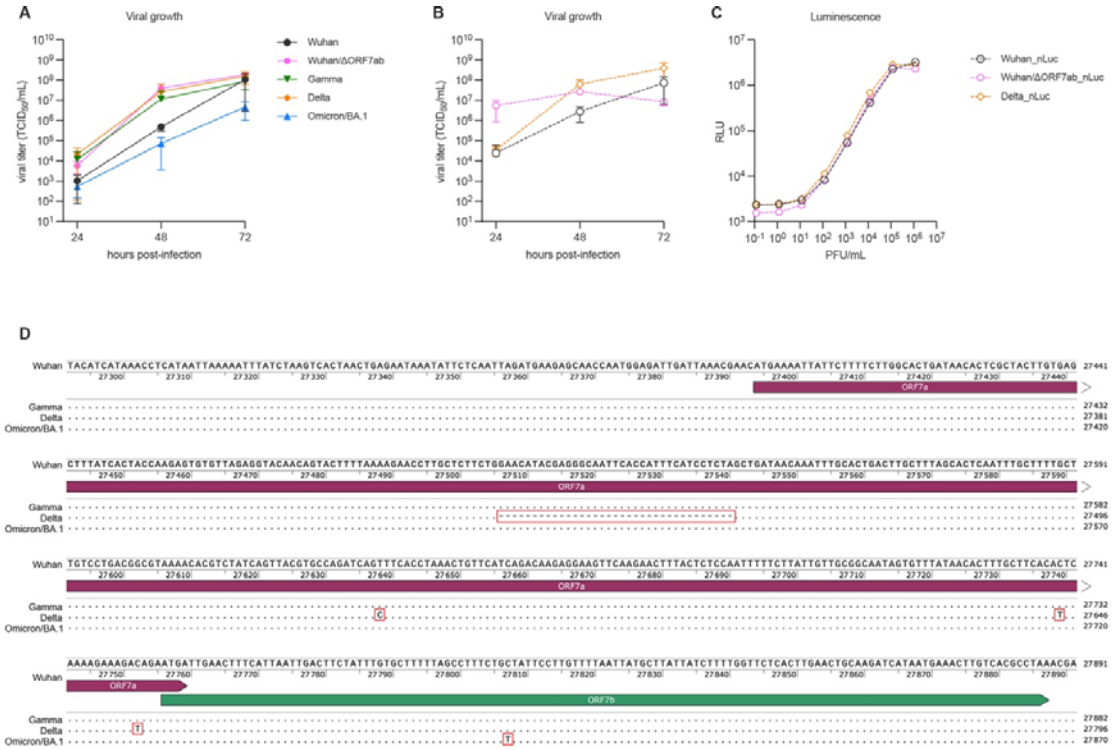

Supplementary Figure 1. *In vitro* viral growth curves of different SARS-CoV-2 viruses. A. Growth curves of the SARS-CoV-2 original virus (Wuhan), the recombinant Wuhan/ΔORF7ab, or the variants of concern (VoC) Gamma, Delta and Omicron/BA.1. **B.** Growth curves of the recombinant nanoluciferase-expressing SARS-CoV-2 viruses Wuhan_nLuc, Wuhan/ΔORF7ab_nLuc, and Delta_nLuc. Horizontal lines indicate median and the interquartile range (n=3 independent replicates/time-point). Viral titers are expressed as the median tissue culture infectious dose ($TCID_{50}$)/mL. **C**. Dilution curves showing the luminescence activity of the recombinant nanoluciferase-expressing SARS-CoV-2 viruses Wuhan_nLuc, Wuhan/ΔORF7ab_nLuc, and Delta_nLuc. RLU: relative light units. **D**. Multiple sequence alignment of the ORF7ab regions of Gamma, Delta and Omicron/BA.1 in comparison with the SARS-CoV-2 original virus (Wuhan). Deletions and mutations are indicated inside red squares. Related to Figures 1, 3, and 4.

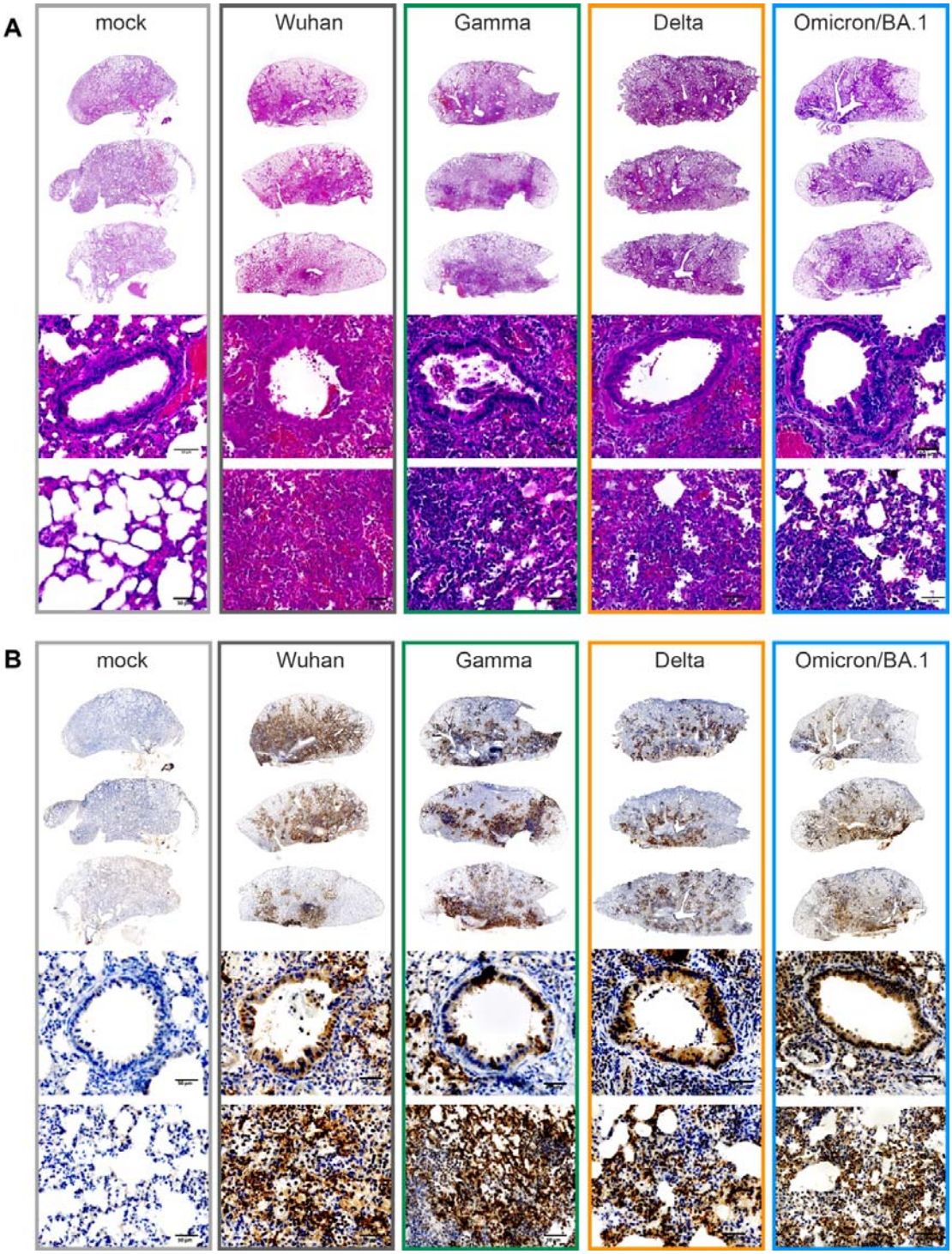

Supplementary Figure 2. Histopathology and immunohistochemical aspects of freshly-collected lungs from hamsters infected with SARS-CoV-2 original virus (Wuhan) or the variants of concern (VoC) Gamma, Delta and Omicron/BA.1 at 4 days post-infection (dpi). A. Representative images of Hematoxylin and Eosin (H&E) stained-whole lung sections (upper panels), bronchiolar epithelium (middle panels) and alveoli (bottom panels). **B.** Representative images of whole lung sections (upper panels), bronchiolar epithelium (middle panels) and alveoli (bottom panels) immuno-stained with SARS-CoV-2 N antibody. Immunoperoxidase, scale bar = 50 µm (n=8/group, except Omicron/BA.1 where n=4). Related to Figure 1.

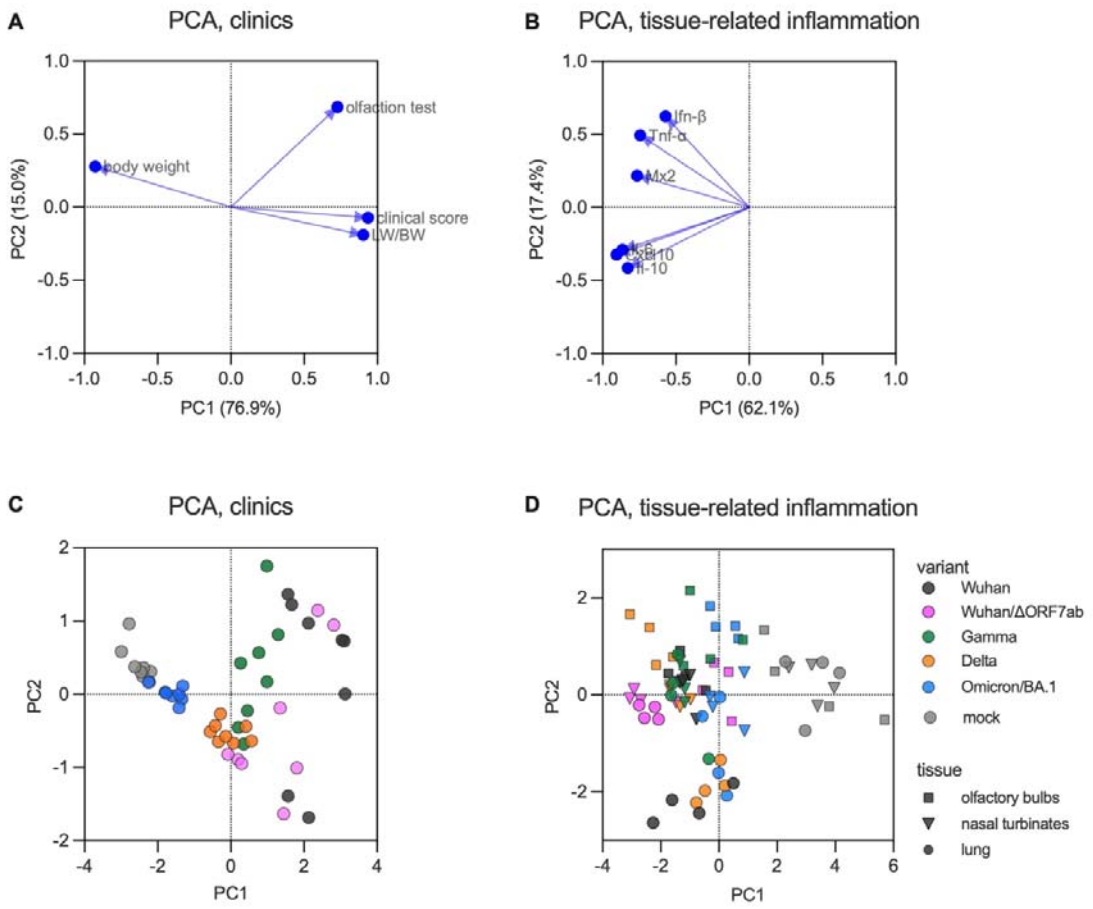

Supplementary Figure 3. Principal component analysis (PCA) of clinical parameters and immune mediators in different tissues of hamsters infected with SARS-CoV-2 original virus (Wuhan), the recombinant Wuhan/ΔORF7ab or the variants of concern (VoC) Gamma, Delta and Omicron/BA.1. A. Variable correlation plot showing the correlation of clinical parameters in hamsters at 4 days post-infection (body weight variation, clinical score, olfaction test and lung weight-to-body weight ratio 'LW/BW'). The two-first principal components explained 92.2% of sample variability (n=8/group). **B.** Variable correlation plot showing the correlation of immune mediators' gene expression (*Mx2, Ifn-β, Il-6, Cxcl10, Tnf-α* and *Il-10*) in the olfactory bulb, nasal turbinates and lungs of hamsters at 4 days post-infection. The two-first principal components explained 80.5% of sample variability (n=4/group). **CD.** PCA plots. Each symbol represents one animal, colored according to the virus variant. Related to Figures 1 and 2.

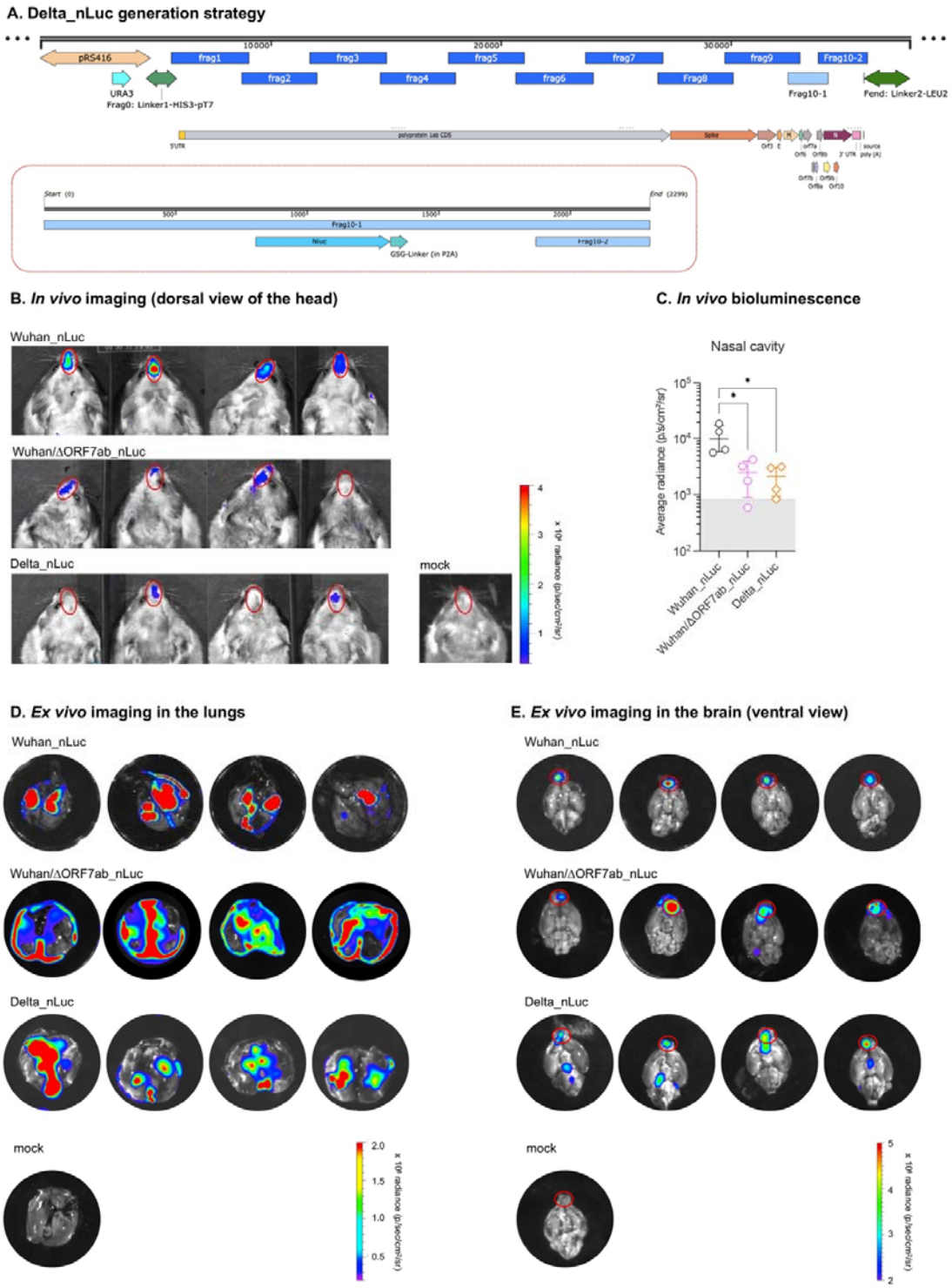

Supplementary Figure 4. *In vivo* and *ex vivo* imaging in hamsters infected with bioluminescent recombinant SARS-CoV-2 viruses at 4 days post-infection (dpi). **A.** Delta_nLuc generation strategy. **B.** *In vivo* imaging of hamsters infected with the recombinant viruses Wuhan_nLuc and Wuhan/ΔORF7ab_nLuc (based on the original SARS-CoV-2 Wuhan) and Delta_nLuc (based on the Delta). The regions of interest (ROIs) are shown as red circles (n=4/group). **C.** *In vivo* bioluminescence values from the nasal cavity (n=4/group). Horizontal lines indicate median and the interquartile range. Kruskal-Wallis test followed by the Dunn's multiple comparisons test (*P<0.05).

469 The gray crosshatched area corresponds to background signals obtained from a mock-infected
470 hamster. **DE.** *Ex vivo* imaging of lungs (D) and brains (E) from hamsters infected with Wuhan_nLuc,
471 Wuhan/ΔORF7ab_nLuc and Delta_nLuc and mock-infected at 4 dpi. The regions of interest (ROIs)
472 are shown as red circles in the olfactory bulbs (for the lungs and the whole brain, the values from
473 the whole organ were acquired). Related to Figure 3.

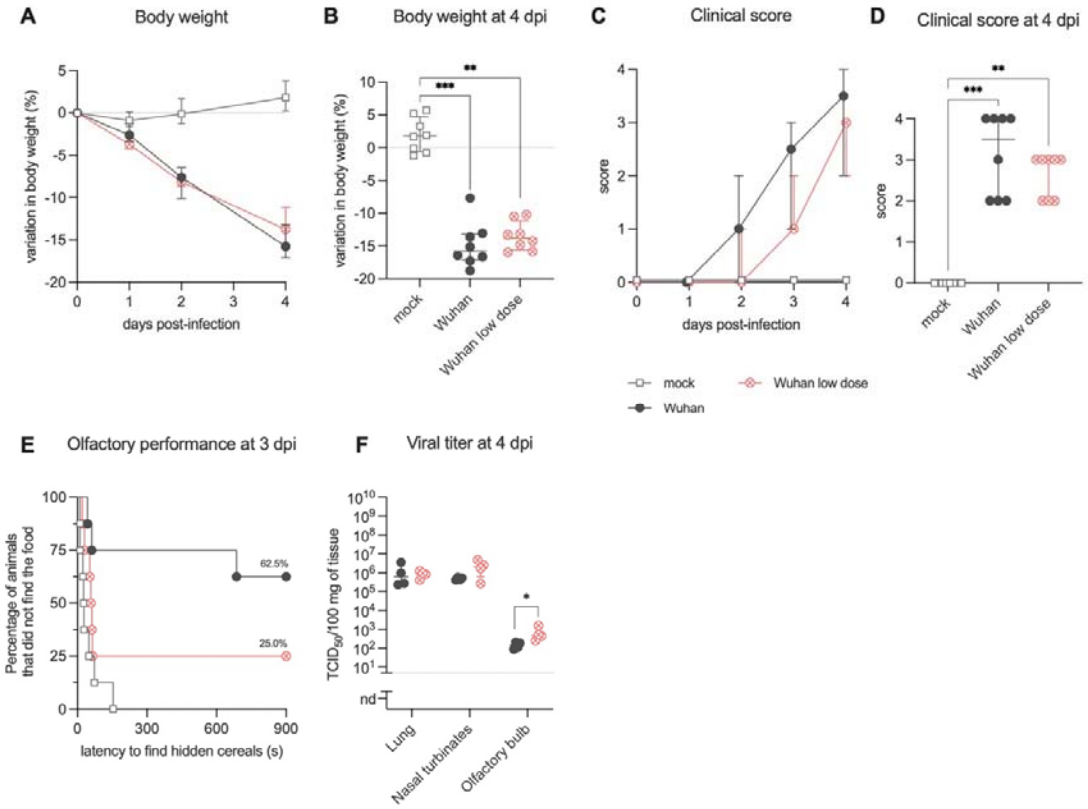

Supplementary Figure 5. Clinical profile of hamsters inoculated with SARS-CoV-2 original virus (Wuhan) with a regular infectious dose (6x10^4 PFU) and with a low infectious dose (6x10^2 PFU). AB. Body weight variation over 4 days post-infection (dpi). **CD.** Clinical score comparison in the acute phase (4 dpi). The clinical score is based on a cumulative 0–4 scale: ruffled fur; slow movements; apathy; and absence of exploration activity. Horizontal lines indicate median and the interquartile range (n=8/group). **E**. Olfactory performance measured at 3 dpi. The olfaction test is based on the hidden (buried) food finding test. Curves represent the olfactory performance of animals during the test (n=8/group). **F**. Infectious viral titers in the lung, nasal turbinates, and olfactory bulbs at 4 dpi expressed as $TCID_{50}$ per 100 mg of tissue. Horizontal lines indicate median and the interquartile range (n=4/group). Kruskal-Wallis test followed by the Dunn's multiple comparisons test (*P<0.05, **P<0.01, ***P<0.001) (A-C) or Mann-Whitney test (*P<0.05) (F). Data for SARS-CoV-2 Wuhan already presented in Figures 1 and 2.

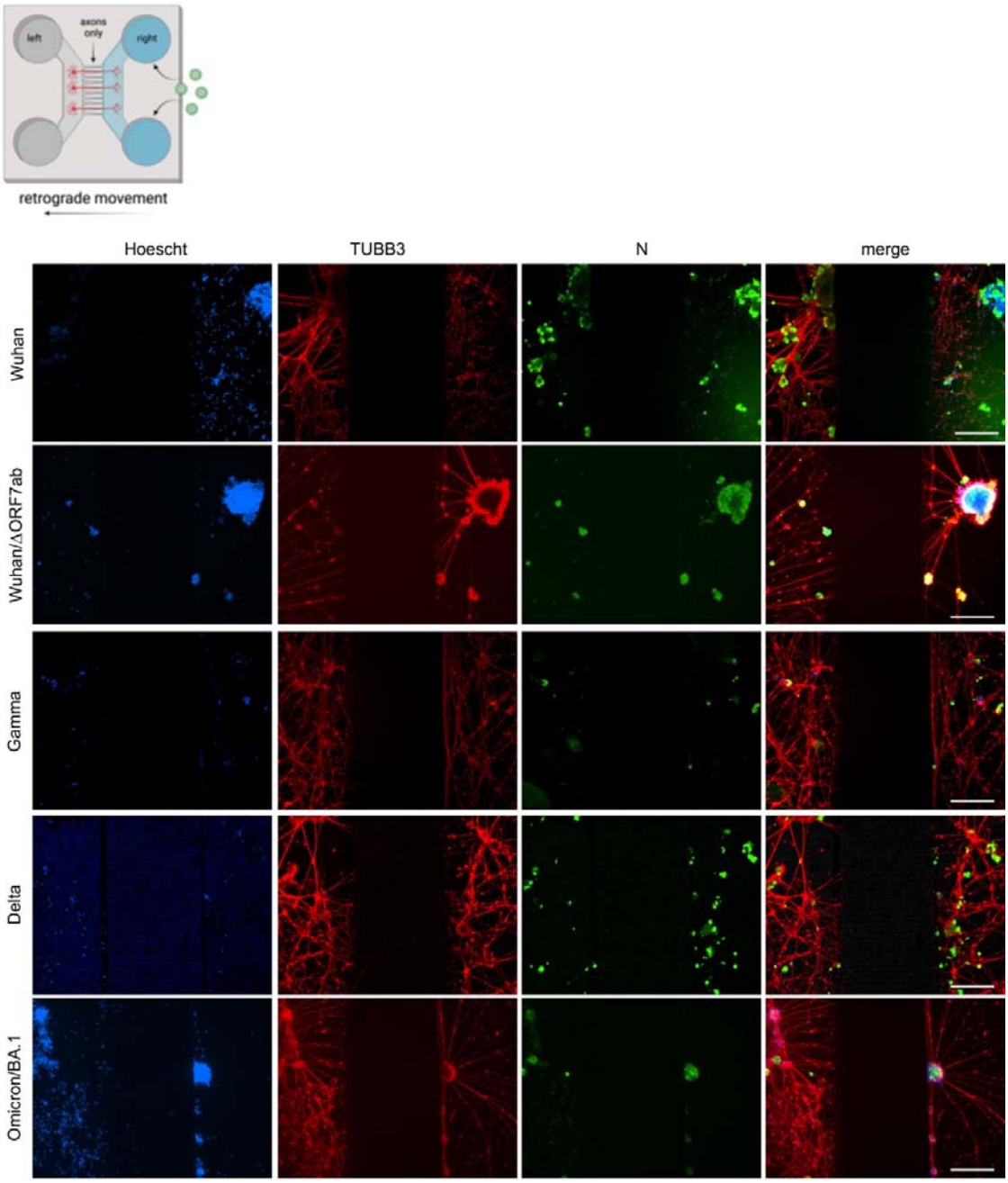

487
488 **Supplementary Figure 6. SARS-CoV-2 travels retrogradely along axons in *in vitro* neuron-epithelial**
489 **networks.** Schematic view of an axon diode in a microfluidic device where the left and the right
490 chambers are connected exclusively by axons. In these images, SARS-CoV-2 was added in the right
491 chamber: Wuhan, Wuhan/ΔORF7ab, Gamma, Delta, and Omicron/BA.1, showing infected cells in
492 both the left and right chambers (scale bar = 200 µm). Hoechst: nuclei (blue). TUBB3: β-Tubulin III
493 (red). N: SARS-CoV-2 nucleocapsid (green). The black zones in the central part of the
494 photomicrographs corresponds to the microchannels, which are not accessible during
495 immunostainings. Related to Figure 4.

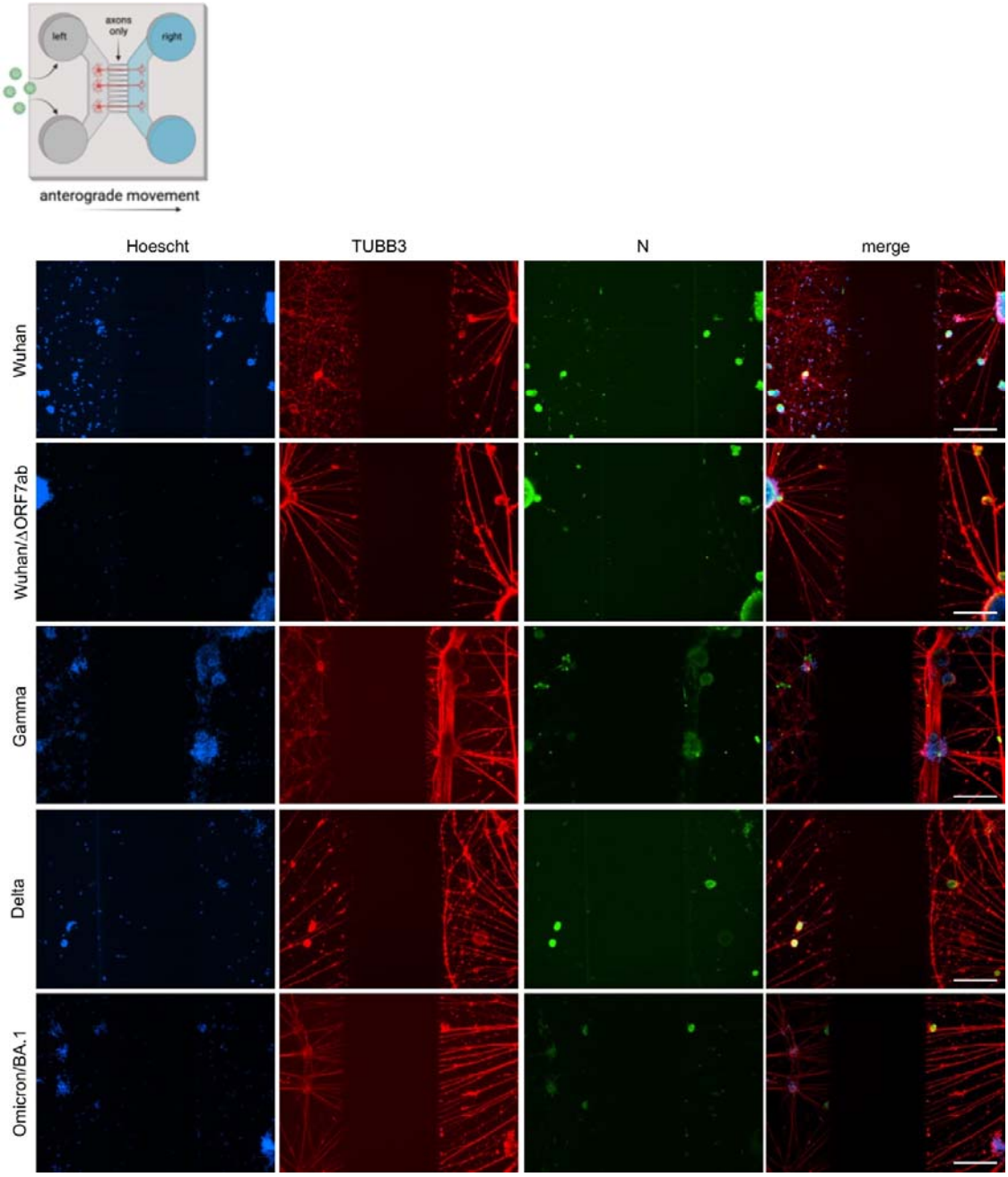

496
497 **Supplementary Figure 7. SARS-CoV-2 travels anterogradely along axons in *in vitro* neuron-**
498 **epithelial networks.** Schematic view of an axon diode in a microfluidic device where the left and
499 the right chambers are connected exclusively by axons. In these images, SARS-CoV-2 was added in
500 the left chamber: Wuhan, Wuhan/ΔORF7ab, Gamma, Delta, and Omicron/BA.1, showing infected
501 cells in both the left and right chambers (scale bar = 200 µm). Hoechst: nuclei (blue). TUBB3: β-
502 Tubulin III (red). N: SARS-CoV-2 nucleocapsid (green). The black zones in the central part of the
503 photomicrographs corresponds to the microchannels, which are not accessible during
504 immunostainings. Related to Figure 4.

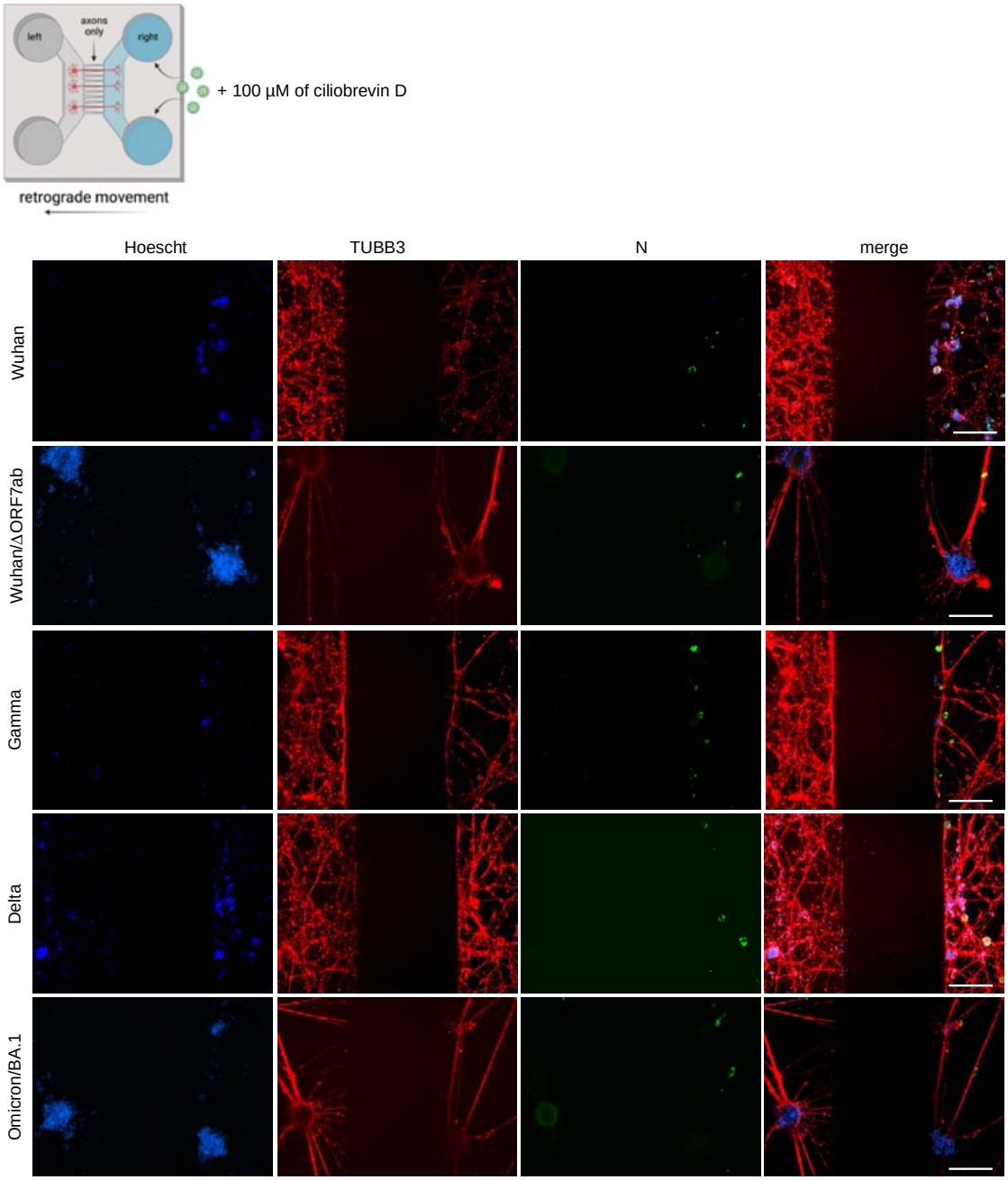

Supplementary Figure 8. SARS-CoV-2 retrograde movement inside axons can be blocked by ciliobrevin D in *in vitro* neuron-epithelial networks. Schematic view of an axon diode in a microfluidic device where the left and the right chambers are connected exclusively by axons. In these images, 100 µM of ciliobrevin was added in both chambers and SARS-CoV-2 was added in the right chamber: Wuhan, Wuhan/ΔORF7ab, Gamma, Delta, and Omicron/BA.1, showing infected cells only in the right chambers (scale bar = 200 µm). Hoechst: nuclei (blue). TUBB3: β-Tubulin III (red). N: SARS-CoV-2 nucleocapsid (green). The black zones in the central part of the photomicrographs corresponds to the microchannels, which are not accessible during immunostainings. Related to Figure 4.

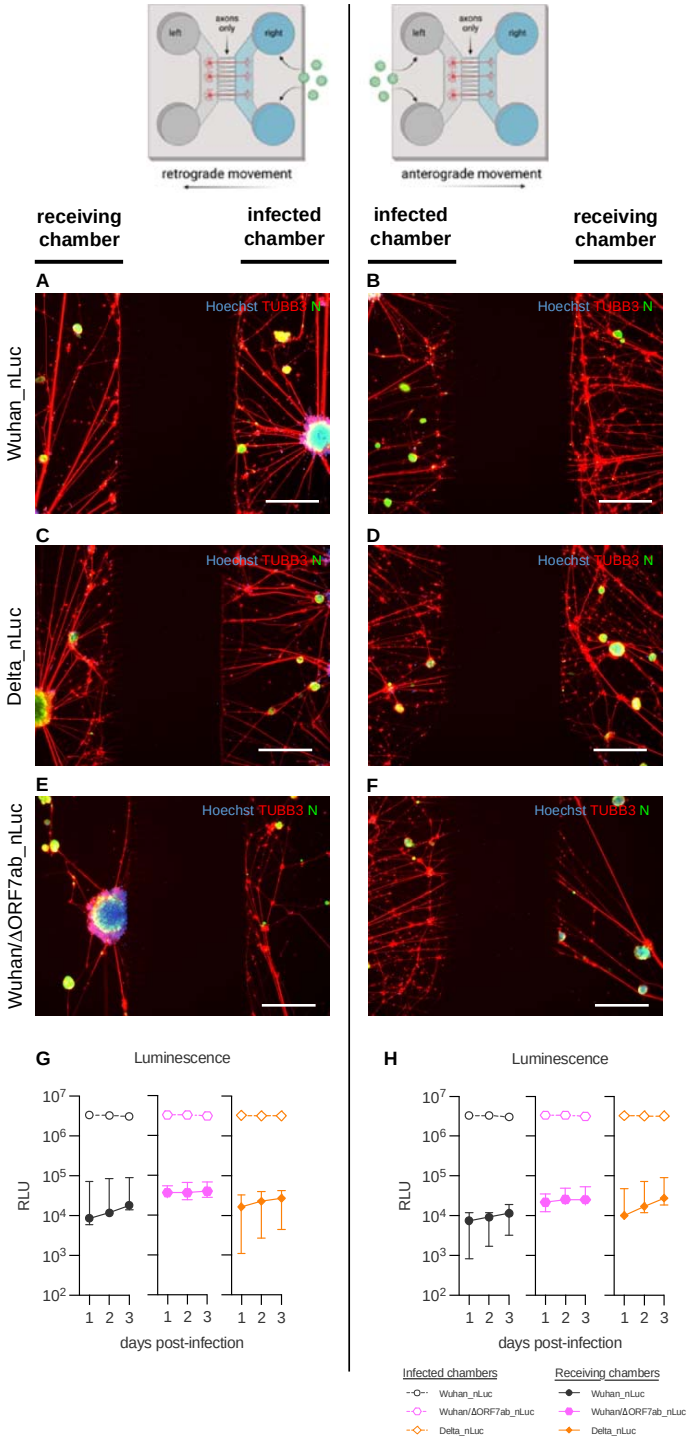

Supplementary Figure 9. Quantification of the intra-axonal traffic of SARS-CoV-2 in *in vitro* neuron-epithelial networks. AF. Photomicrographs of retrograde (A,C,E) and anterograde (B, D, F) movement of the recombinant viruses Wuhan_nLuc (AB), Wuhan/ΔORF7ab_nLuc (CD) and Delta_nLuc (EF) at 3 dpi (scale bar = 200 µm). Hoechst: nuclei (blue). TUBB3: β-Tubulin III (red). N: SARS-CoV-2 nucleocapsid (green). **GH.** SARS-CoV-2 quantification by sequential luminescence measurements in the supernatants, in the retrograde (G) or anterograde (H) directions (n=3 independent replicates). Open symbols indicate the infected chambers, full-colored symbols indicate the chambers receiving the virus via the axons. RLU: relative light units. Related to Figure 4.

524 **Supplementary Video 1. Light sheet imaging in the nasal turbinates and in the olfactory bulbs.** 3D
525 distribution of the nucleocapsid in the nostrils, including the olfactory mucosa, in the olfactory
526 nerve and in neurons in the olfactory bulbs of a SARS-CoV-2 Wuhan infected hamster using whole-
527 head clearing. Related to Figure 3.

528 **Supplementary Table 1. Primer sequences used to amplify the different fragments for yeast**
529 **recombination.**
530

Fragment	Sequence (5'-3') *		Position on the viral genome	Size
pRS416	Forward	CCAGTAATGTGGACATTGCC	/	4816
	Reverse	CATCAACGACCTTGTCTTCAGTA	/	
Linker His3	Forward	CCTGAAAGCACTTGAAGAATTCC	/	1448
	Reverse	GGTATGCTAAGGCACAGCACACT	78	
Frag1	Forward	GCCATTCATCCACAGTTGACA	in *HIS*3	3213
	Reverse	CATGGTGCTGACAGTGGAGTCT	3183	
Frag2	Forward	TGAGCCATCGTGCCAATG	2885	3251
	Reverse	AGCCCGTCTGCTGGTATCAC	6135	
Frag3	Forward	GGTTGCCAAACCTTATCAGAAATG	5804	3339
	Reverse	TTCACCTGTTCCACAGCCTTG	9142	
Frag4	Forward	ACAGAGAGAAGATGACGCAGATAATG	8885	3251
	Reverse	GCCTGAATGGCCACGTACA	12135	
Frag5	Forward	TGCGGATGATATCTCAACTTTAACTG	11824	3311
	Reverse	AAAGGAAAGCAAAGTTTGTATTGTCA	15134	
Frag6	Forward	TGCGGATGATATCTCAACTTTAACTG	14782	3350
	Reverse	AAAGGAAAGCAAAGTTTGTATTGTCA	18131	
Frag7	Forward	TGCGGATGATATCTCAACTTTAACTG	17786	3371
	Reverse	AAAGGAAAGCAAAGTTTGTATTGTCA	21156	
Frag8	Forward	TGCGGATGATATCTCAACTTTAACTG	20932	3276
	Reverse	AAAGGAAAGCAAAGTTTGTATTGTCA	24207	
Frag9	Forward	TGCGGATGATATCTCAACTTTAACTG	23854	3253
	Reverse	AAAGGAAAGCAAAGTTTGTATTGTCA	28832	
Frag10-1	Forward	TGCGGATGATATCTCAACTTTAACTG	26589	1720
nLuc	Reverse	AAAGGAAAGCAAAGTTTGTATTGTCA	28332	
Frag10-2	Forward	TGCGGATGATATCTCAACTTTAACTG	27903	2132
	Reverse	AAAGGAAAGCAAAGTTTGTATTGTCA	in *LEU*2	
Linker Leu2	Forward	TGCGGATGATATCTCAACTTTAACTG	/	2041
	Reverse	AAAGGAAAGCAAAGTTTGTATTGTCA	/	

531 *Based on the sequence of SARS-CoV-2 Delta/2021/I7.2 200 (GISAID ID: EPI_ISL_2029113) [70]
532

533 **Supplementary Table 2. Primer sequences used for qPCR in the golden hamster tissues.**
534

Gene	Sequence (5'-3')		Reference
Mx2	Forward	CCAGTAATGTGGACATTGCC	[71]
	Reverse	CATCAACGACCTTGTCTTCAGTA	
	Probe	FAM-TGTCCACCAGATCAGGCTTGGTCA-TAMRA	
Ifn-β	Forward	ACCCTAAAGGAAGTGCCAGA	[72]
	Reverse	CCAGCTGCCAGTAATAGCTC	
	Probe	FAM-AGTTTGACTACAAGGATTAGCTTGAA-TAMRA	
Il-6	Forward	CCTGAAAGCACTTGAAGAATTCC	[71]
	Reverse	GGTATGCTAAGGCACAGCACACT	
	Probe	FAM-AGAAGTCACCATGAGGTCTACTCGGCAAAA-TAMRA	
Cxcl10	Forward	GCCATTCATCCACAGTTGACA	[71]
	Reverse	CATGGTGCTGACAGTGGAGTCT	
	Probe	FAM-CGTCCCGAGCCAGCCAACGA-TAMRA	
Tnf-α	Forward	TGAGCCATCGTGCCAATG	[73]
	Reverse	AGCCCGTCTGCTGGTATCAC	
	Probe	FAM-CGGCATGTCTCTCAAAGACAACCAG-TAMRA	
Il-10	Forward	GGTTGCCAAACCTTATCAGAAATG	[73]
	Reverse	TTCACCTGTTCCACAGCCTTG	
	Probe	FAM-TGCAGCGCTGTCATCGATTTCTCCC-TAMRA	
γ-actin	Forward	ACAGAGAGAAGATGACGCAGATAATG	[73]
	Reverse	GCCTGAATGGCCACGTACA	
	Probe	FAM-TTG AAA CCT TCA ACA CCC CAG CC-TAMRA	
Hprt	Forward	TGCGGATGATATCTCAACTTTAACTG	[71]
	Reverse	AAAGGAAAGCAAAGTTTGTATTGTCA	
	Probe	FAM-AAAGAATGTCTTGATTGTTGAAGGTAAAACTGACATTGG-TAMRA	

535

536 **Materials and methods**
537
538 **Ethics**. All animal experiments were performed according to the French legislation and in
539 compliance with the European Communities Council Directives (2010/63/UE, French Law 2013–
540 118, February 6, 2013) and according to the regulations of Institut Pasteur Animal Care
541 Committees. The Animal Experimentation Ethics Committee (CETEA 89) of the Institut Pasteur
542 approved this study (200023; APAFIS#25326-2020050617114340 v2) before experiments were
543 initiated. Hamsters were housed by groups of 4 animals in isolators and manipulated in class III
544 safety cabinets in the Pasteur Institute animal facilities accredited by the French Ministry of
545 Agriculture for performing experiments on live rodents. All animals were handled in strict
546 accordance with good animal practice.
547
548 **SARS-CoV-2 virus and variants.** The isolate BetaCoV/France/IDF00372/2020 (EVAg collection, Ref-
549 SKU: 014V-03890) was kindly provided by the National Reference Centre for Respiratory Viruses
550 hosted by Institut Pasteur (Paris, France) and headed by Pr. Sylvie van der Werf. The human sample
551 from which strain hCoV-19/Japan/TY7-501/2021 (Brazilian variant, JPN [P.1]) was supplied by the
552 Japanese National Institute of Infectious Diseases (Tokyo, Japan). The isolate SARS-CoV-2
553 Delta/2021/I7.2 200 (Indian variant, GISAID ID: EPI_ISL_2029113) and the isolate SARS-CoV-2
554 Omicron/B.1.1.529 (Omicron BA.1 variant, GISAID ID: EPI_ISL_6794907) were kindly provided by
555 the Virus and Immunity Unit hosted by Institut Pasteur and headed by Olivier Schwartz [70,74]. Viral
556 stocks were produced on Vero-E6 cells infected at a multiplicity of infection of $1x10^{-4}$ PFU/cell. The
557 virus was harvested 3 days post-infection, clarified and then aliquoted before storage at -80°C. Viral
558 stocks were titrated on Vero-E6 cells by classical plaque assays using semisolid overlays (Avicel,
559 RC581-NFDR080I, DuPont) [75].
560 Recombinant viruses expressing Nanoluciferase (nLuc) as a reporter gene were obtained by reverse
561 genetics. Wuhan_nLuc was derived from the clone synSARS-CoV-2-GFP-P2A-ORF7a (clone #41)
562 generated as described [76-80], where the GFP reporter gene was replaced by the nLuc one. The
563 cloning strategy was optimized to build a complete cDNA of the Delta_nLuc virus on the same
564 backbone than the isolate EPI_ISL_2029113. SARS-CoV-2 Wuhan/ΔORF7ab was obtained using the
565 same reverse genetic system by replacing the complete ORF7ab sequence by that of GFP or by nLuc
566 (Wuhan/ΔORF7ab_nLuc).
567
568 **Generation of the complete genome of SARS- CoV-2/Delta_nLuc virus.** The viral genome was
569 divided in 11 overlapping fragments around 3kb each. Those fragments and two fragments coding
570 for different yeast-specific selection genes (His3 and Leu2) were recombined in the yeast

571 centromere plasmid pRS416 to generate the complete genome clone of recombinant virus. The T7
572 promotor was placed just before the 5'UTR sequence and a unique restriction site EAG1 was placed
573 just after the poly(A) tail.
574 Viral fragments were obtained either by RT-PCR on RNA extracted from Vero-E6 cells infected by
575 Delta using the SuperScript IV VILO Master Mix (11756050, Thermofisher) according to the
576 manufacturer protocol, or using synthetic genes (GeneArt, Life Technologies). All PCR
577 amplifications were performed using Phusion™ High-Fidelity DNA Polymerase (F530, Thermofisher).
578 The PCR product were cloned in Topo-TA vector and their sequences controlled by sanger
579 sequencing. The nLuc gene was inserted upstream ORF7a and separated from it using a GSG linker
580 and a P2A peptide sequence to mediate cleavage between the reporter and the viral protein. It was
581 directly synthetized in the F10-1 fragment.
582
583 **Yeast recombination.** Recombination of the 4 yeast specific fragments and the 11 viral fragments
584 was performed on *S. cerevisiae* BY4741. A yeast culture was carried out from an overnight pre-
585 culture in YPDA medium (2 mL of pre-culture in 50 mL of YPDA medium heated to 30° C) until the
586 exponential growth phase was reached, with an optical density corresponding to approximately 10^8
587 cells/mL. The yeasts were harvested by centrifugation of 50 mL of culture (5,000 rpm at 4°C during
588 5 min) before being washed a first time in sterile solution of Tris-EDTA and lithium Acetate TE/LiAc
589 (Tris-HCl pH 7.5 10 mM; EDTA pH 7.5 0.1 mM; LiAc 100 mM). Cells were resuspended in 500 µL of
590 TE/LiAc solution (2.10^9 cells/mL). The yeast suspension was then incubated at 30° C without stirring
591 during 30 min. During this time, a mix of all DNA fragments in an equimolar proportion was
592 prepared. For each recombination condition, 50 µL of competent cells (10^8 cells) were resuspended
593 in a final volume of 300 µL TE/LiAc/PEG solution (100 mM Tris-HCl pH 8; 100 mM Lithium Acetate;
594 40% v/v PEG 3350) with the DNA mix to be recombined and 50 µg of denaturated salmon sperm
595 DNA (31149, Sigma) and then cooled on ice for 5 min. The mixture was incubated at 30°C during 30
596 min without agitation before undergoing a heat shock at 42°C during 20 min. After cooling on ice,
597 the yeasts were pelleted by centrifugation at 2,000 rpm at RT during 5 min and then resuspended
598 and incubated with 500 µL of 5 mM $CaCl_2$ at RT for 10 min. $CaCl_2$ was washed by centrifugation at
599 2,000 rpm at RT during 5 min and cells were resuspended in 200 µL of sterile water before being
600 plated on selective synthetic minimal medium lacking histidine, Uracyl and Leucine (SD-His-Ura-
601 Leu-), and incubated at 30°C for 3 days. For each transformation, ten different clones were checked
602 by multiplex PCR (206143, Qiagen) on rapid DNA preparations carried out by the Chellex technique
603 as already described [76] using specific primers (Table S1) to control the presence of the different
604 fragments in the expected orientation. The yeast colony of interest was sub-cultured in 200 mL of

605 SD-His-Ura-Leu- medium and the plasmid extracted using the Qiagen midi prep kit (12143, Qiagen)
606 following manufacturer's instructions.
607
608 **Rescue of the virus.** The plasmid was linearized by EagI-HF (R3505, NEB) digestion, purified by a
609 phenol chloroform process and transcribed *in vitro* into RNA using the T7 RiboMaxTM Large Scale
610 RNA Production System (P1300, Promega) and the m7G(5')ppp(5')G RNA Cap Structure Analog
611 (#S1411, NEB) kits. Approximately 5 µg of linear DNA were used as template in a reaction volume of
612 50 µL comprising: 10 µL of 5X T7 transcription buffer; 5 µL of m7G(50)ppp(50)G RNA cap analog
613 structure at 30 mM; 0.75 µL of 100 mM GTP; 3.75 µL of each nucleotide type ATP, CTP; 100 mM
614 UTP; and 5 µL of RNasin T7 RNA polymerase enzyme. The reaction was incubated at 30°C during 3 h
615 then the template DNA was digested at 37°C during 20 min by adding 2 µL of the enzyme RQ1
616 RNase free DNase. The synthesized RNA was finally purified using a classical phenol chloroform
617 method and precipitated. Twelve µg of complete viral mRNA and 4 µg of plasmid encoding the viral
618 nucleoprotein (N) gene were electroporated on $8x10^6$ Vero-E6 cells resuspended in 0.8 mL of Mirus
619 Bio™ Ingenio™ Electroporation Solution (MIR50114) using the Gene Pulser Xcell Electroporation
620 System (1652660, Biorad) with a pulse of 270V and 950 µF. The cells were then transferred to a T75
621 culture flask with 15 mL of DMEM supplemented with 2% FCS (v/v). The electroporated cells were
622 incubated at 37°C, 5% CO_2 for several days until the cytopathic effect (CPE) was observed. Then, the
623 supernatant was harvested, aliquoted and frozen at -80°C until titration. The viral sequence was
624 controlled by NGS.
625
626 **Viral growth curves.** Vero-E6 cells (ATCC CRL-1586) were used to assess the replication kinetics of
627 different SARS-CoV-2 variants and recombinant viruses. The cells were maintained in Dulbecco's
628 modified culture medium (DMEM, 31966-021, Gibco) supplemented with 5% fetal calf serum, at
629 37°C in 5% CO_2. On the day before infection, $1x10^6$ VeroE6 cells/well were plated onto 6-well
630 plates. On day of infection, the cells were infected with SARS-CoV-2 virus at a multiplicity of
631 infection (MOI) of 0.01, in independent triplicates, and incubated during 24-, 48- or 72-hours post-
632 infection. The supernatants were collected at each time-point and frozen at -80°C. Viral titers were
633 obtained by classical $TCID_{50}$ method on Vero-E6 cells after 72 hours post-infection [81].
634
635 **SARS-CoV-2 model in golden Syrian hamsters.** Male golden Syrian hamsters (*Mesocricetus auratus;*
636 RjHan:AURA) of 5-6 weeks of age (average weight 60-80 grams) were purchased from Janvier
637 Laboratories and handled under specific pathogen-free conditions. The animals were housed and
638 manipulated in isolators in a biosafety level-3 facility, with *ad libitum* access to water and food.
639 Before any manipulation, animals underwent an acclimation period of one week. Animals were

640 anesthetized with an intraperitoneal injection of 200 mg/kg ketamine (Imalgène 1000, Merial) and
641 10 mg/kg xylazine (Rompun, Bayer), and 100 µL of physiological solution containing $6x10^4$ PFU of
642 SARS-CoV-2 (wild-type or recombinant) was administered intranasally to each animal (50
643 µL/nostril). Mock-infected animals received the physiological solution only. Infected and mock-
644 infected hamsters were housed in separate isolators and were followed-up daily during four days at
645 which the body weight and the clinical score were noted. The clinical score was based on a
646 cumulative 0-4 scale: ruffled fur, slow movements, apathy, absence of exploration activity. At day 3
647 post-infection (dpi), animals underwent a food finding test to assess olfaction as previously
648 described [14,82]. Briefly, 24 hours before testing, hamsters were fasted and then individually placed
649 into a fresh cage (37 x 29 x 18 cm) with clean standard bedding for 10 minutes. Subsequently,
650 hamsters were placed in another similar cage for 2 minutes when about 5 pieces of cereals were
651 hidden in 1.5 cm bedding in a corner of the test cage. The tested hamsters were then placed in the
652 opposite corner and the latency to find the food (defined as the time to locate cereals and start
653 digging) was recorded using a chronometer. The test was carried out during a 15 min period. As
654 soon as food was uncovered, hamsters were removed from the cage. One minute later, hamsters
655 performed the same test but with visible chocolate cereals, positioned upon the bedding. The tests
656 were realized in isolators in a Biosafety level-3 facility that were specially equipped for that. At 4
657 dpi, animals were euthanized with an excess of anesthetics (ketamine and xylazine) and
658 exsanguination [83], and samples of nasal turbinates, lungs and olfactory bulbs were collected and
659 immediately frozen at -80°C. Fragments of lungs were also collected and fixed in 10% neutral-
660 buffered formalin.
661
662 **SARS-CoV-2 detection in golden hamsters' tissues.** Frozen lung fragments, nasal turbinates and
663 olfactory bulbs were weighted and homogenized with 1 mL of ice-cold DMEM supplemented with
664 1% penicillin/streptomycin (15140148, Thermo Fisher) in Lysing Matrix M 2 mL tubes (116923050-
665 CF, MP Biomedicals) using the FastPrep-24™ system (MP Biomedicals), and the following scheme:
666 homogenization at 4.0 m/s during 20 sec, incubation at 4°C during 2 min, and new homogenization
667 at 4.0 m/s during 20 sec. The tubes were centrifuged at 10.000 x g during 2 min at 4°C, and the
668 supernatants collected. Viral titers were obtained by classical $TCID_{50}$ method on Vero-E6 cells after
669 72 hours post-infection [81]. Viral RNA loads were obtained by the quantification of genomic and sub-
670 genomic SARS-CoV-2 RNA based on the E gene [84]. Briefly, 125 µL of the supernatants were
671 homogenized with 375 µL of Trizol LS (10296028, Invitrogen) and total RNA was extracted using the
672 Direct-zol RNA MicroPrep Kit (R2062, Zymo Research: nasal turbinates and olfactory bulbs) or
673 MiniPrep Kit (R2052, Zymo Research: lung). We used the Taqman one-step qRT-PCR (Invitrogen
674 11732-020) in a final volume of 12.5 µL per reaction in 384-wells PCR plates using a thermocycler

675 (QuantStudio 6 Flex, Applied Biosystems). Briefly, 2.5 µL of RNA were added to 10 µL of a master
676 mix containing 6.25 µL of 2X reaction mix, 0.2 µL of $MgSO_4$ (50 mM), 0.5 µL of Superscript III
677 RT/Platinum Taq Mix (2 UI/µL) and 3.05 µL of nuclease-free water containing 400 nM of primers
678 and 200 nM of probe. To detect the genomic RNA, we used the E_sarbeco primers and probe
679 (E_Sarbeco_F1 5'-ACAGGTACGTTAATAGTTAATAGCGT-3'; E_Sarbeco_R2 5'-
680 ATATTGCAGCAGTACGCACACA-3'; E_Sarbeco_Probe FAM-5'-ACACTAGCCATCCTTACTGCGCTTCG-3'-
681 TAMRA). The detection of sub-genomic SARS-CoV-2 RNA was achieved by replacing the
682 E_Sarbeco_F1 primer by the CoV2sgLead primer (CoV2sgLead-Fw 5'-
683 CGATCTCTTGTAGATCTGTTCTC-3'). A synthetic gene encoding the PCR target sequences was
684 ordered from Thermo Fisher Scientific. A PCR product was amplified using Phusion™ High-Fidelity
685 DNA Polymerase (Thermo Fisher Scientific) and *in vitro* transcribed by means of Ribomax T7 kit
686 (Promega). RNA was quantified using Qubit RNA HS Assay kit (Thermo Fisher scientific), normalized,
687 and used as a standard to quantify RNA absolute copy number. The amplification conditions were
688 as follows: 55°C for 20 min, 95°C for 3 minutes, 50 cycles of 95°C for 15 s and 58°C for 30 s;
689 followed by 40°C for 30 s.
690
691 **Transcriptomics analysis in golden hamsters' tissues.** RNA preparations from lungs, nasal
692 turbinates and olfactory bulbs collected at 4 dpi were submitted to RT-qPCR. Briefly, RNA was
693 reverse transcribed to first strand cDNA using the SuperScript™ IV VILO™ Master Mix (11766050,
694 Invitrogen). qPCR was performed in a final volume of 10 µL per reaction in 384-well PCR plates
695 using a thermocycler (QuantStudio 6 Flex, Applied Biosystems). Briefly, 2.5 µL of cDNA (12.5 ng)
696 were added to 5 µL of Taqman Fast Advanced master mix (444457, Applied Biosystems) and
697 2.5 µL of nuclease-free water containing golden hamster's primer pairs (Table S2). The
698 amplification conditions were as follows: 95°C for 20 s, and 45 cycles of 95°C for 1 s and 60°C for
699 20 s. The *γ-actin* and the *Hprt* (hypoxanthine phosphoribosyl-transferase) genes were used as
700 reference. Variations in gene expression were calculated as the n-fold change in expression in the
701 tissues from the infected hamsters compared with the tissues of the mock-infected group using the
702 $2^{-\Delta\Delta Ct}$ method [85].
703
704 **Sample staining and iDISCO+ clearing.** For iDISCO+, three male and three female hamsters were
705 infected with $6x10^4$ PFU of SARS-CoV-2 Wuhan and followed up as described above. At 4 dpi,
706 animals were anesthetized with an intraperitoneal injection of ketamine (200 mg/kg; Imalgène
707 1000, Merial) and xylazine (10 mg/kg; Rompun, Bayer), and we performed a transcardial perfusion
708 with DPBS containing heparin (5×10^3 U/mL) followed by 4% neutral-buffered formaldehyde. The
709 whole heads were collected and stored in 4% neutral-buffered formaldehyde during one week

710 before analysis. SARS-CoV-2 nucleocapsid was detected *in toto* in the snout and brain of infected
711 hamsters using the iDISCO+ protocol previously published [86] with minimal modifications. All buffers
712 were supplemented with 0,01% of sodium azide (Sigma-Aldrich). The snout, containing the
713 olfactory mucosa and the olfactory nerve, and the brain were dissected and processed separately
714 to optimize tissue manipulation.
715 All samples were first dehydrated in methanol (Sigma-Aldrich) using 20-40-60-80-100-100%
716 dilutions in distilled water (1h to 2h each concentration). Complex lipid removal was achieved
717 incubating the samples in a 2:1 mixture of dichloromethane (Sigma-Aldrich) and methanol
718 overnight. Samples were then washed twice in methanol 100% and bleached overnight using a
719 H_2O_2 5% solution in methanol. Then all samples were rehydrated using a methanol series (80-60-
720 40-20%). To increase bone permeability, the snouts were decalcified by incubation in the Morse's
721 solution (formic acid 45% and sodium citrate 20%). Finally, all the samples (brains and snouts) were
722 washed in PBS, then PBS-T (PBS with 0,2% Triton X-100 [Sigma-Aldrich]) and incubated in
723 permeabilization buffer (20% DMSO [Sigma-Aldrich] and 2.3% glycine [Sigma-Aldrich] in PBS-T) at
724 37°C overnight. Before immunostaining, samples were blocked (0,2% Gelatin [Sigma-Aldrich] in
725 PBS-T) at 37°C for 24h. To reveal SARS-CoV-2 and vasculature, three primary antibodies were
726 combined: Rabbit anti-SARS CoV2 nucleocapsid antibody (GTX135357, GeneTex) diluted 1:1000;
727 Goat anti-CD31 (AF3628, R&D Systems) diluted 1:300; and Rat anti-Podocalyxin (MAB1556, R&D
728 Systems) diluted 1:1000. After a 2-weeks incubation in primary antibody, the samples were washed
729 (PBS supplemented with 0,2% tween-20 [Sigma-Aldrich] and 2U/mL heparin [Sigma-Aldrich]) and
730 incubated 10 days with the following secondary antibodies: Donkey anti-Rabbit Alexa 555 (A-31572,
731 Thermo Fisher Scientific), Donkey anti-Goat Alexa 647 (A-21447, Thermo Fisher Scientific) and
732 Chicken anti-Rat Alexa 647 (A-21472, Thermo Fisher Scientific) all diluted at 1:500. All antibodies
733 were diluted in blocking solution and incubated at 37°C with gentle shacking. After
734 immunostaining, the samples were washed, dehydrated in methanol (20-40-60-80-100-100%),
735 incubated for 3h in a 2:1 mixture of dichloromethane and methanol, washed twice (15 min each) in
736 dichloromethane 100% and cleared by immersion in dibenzyl ether.
737
738 **Light sheet imaging.** Brain and snout samples were imaged using a LaVision Ultramicroscope II
739 equipped with infinity-corrected objectives, laser lines OBIS-561nm 100mW and OBIS-639nm
740 70mW, and 595/40 and 680/30 filters for Alexa 555 and Alexa 647 respectively. The olfactory bulbs
741 were imaged with a 4X 0,35NA objective, using a laser NA of 0,3 and a step size of 2µm obtaining
742 images with 1,63x1,63x2µm/pixel resolution. The snouts were imaged with a 1,3X objective,
743 adjusting the laser NA to 0,3 and step size of 5µm obtaining images with a 5x5x5µm/pixel

744 resolution. All acquisitions were done with LaVision BioTec ImSpector Software. The 3D stacks
745 obtained were analyzed using Bitplane Imaris 9.2 (Oxford instruments).
746
747 ***In vivo* and *ex vivo* bioluminescence imaging.** At 4 dpi, animals infected with SARS-CoV-
748 2/Wuhan_nLuc, Wuhan/ΔORF7ab_nLuc and SARS-CoV-2/Delta_nLuc were anesthetized with an
749 intraperitoneal injection of ketamine (200 mg/kg; Imalgène 1000, Merial) and xylazine (10 mg/kg;
750 Rompun, Bayer). Next, 0.45 µmoles of the nLuc substract (Nano-Glo® *in vivo* substrate, CS320501,
751 Promega) fluorofurimazine (FFz) were injected interperitoneally and the animals were placed in a
752 confinement box and imaged using an IVIS® Spectrum *In Vivo* Imaging System (PerkinElmer) within
753 5 minutes of FFz injection. Two-dimensional bioluminescence images were recorded, and photon
754 emission was quantified (p/s/cm^2/sr) in a region of interest defined using Living Image software
755 (PerkinElmer). After *in vivo* imaging, animals were euthanized, the lungs and the brains were
756 collected and quickly placed in a six-wells plate. The plates were placed in a confinement box and
757 imaged as described above.
758
759 **Histopathology and Immunohistochemistry.** Lung fragments fixed 7 days in 10% neutral-buffered
760 formalin were embedded in paraffin. Four-µm-thick sections were cut and stained with
761 hematoxylin and eosin staining. IHC were performed on Leica Bond RX using anti SARS
762 Nucleocapsid Protein antibody (NB100-56576, Novus Biologicals) and biotinylated goat anti-rabbit
763 Ig secondary antibody (E0432, Dako, Agilent). Slides were then scanned using Axioscan Z1 slide
764 scanner (Zeiss) and images were analyzed with the Zen 2.6 software (Zeiss).
765
766 **Neuron-epithelial networks in microfluidic chambers.** Human neural stem cells (hNSC,
767 ENStem-A, SCC003, EMD-Millipore) were maintained in geltrex-coated 6-well plates (A1413302,
768 Gibco) in a density of 4.5x10^5 cells/cm^2 in CTS Knock-out DMEM/F12 medium (A1370801, Gibco)
769 supplemented with 2% StemPro neural supplement (A1050801, Gibco), 2 mM glutamax (35050038,
770 Gibco), 20 ng/mL FGFb (PHG0026, Gibco) and 20 ng/mL EGF (PHG0311, Gibco) at 37°C in 5% CO_2.
771 A549-ACE2-TMPRSS2 cells (kindly provided by Pr. Olivier Schwartz, Institut Pasteur) were
772 maintained in F12K Nut Mix medium (21127022, Gibco) supplemented with 10% bovine calf serum
773 and 10 µg/mL blasticidine (12172530, Gibco) at 37°C in 5% CO_2. To generate the neuron-epithelial
774 networks, we used microfluidic chips purchased from MicroBrain Biotech (Brainies™, Cat#: MBBT5;
775 Marly le Roi, France). Brainies™ MBBT5 is a chip containing 4 neuronal diodes. One neuronal diode
776 includes 2 rectangular culture chambers (volume ~1 µL) each connected to 2 reservoirs and
777 separated by a series of 500 µm-long asymmetrical micro-channels (3 µm high, tapering from 15
778 µm to 3 µm) [33]. Brainies™ were coated with poly-L-ornithine (P4957, Sigma-Aldrich) and laminin

779 (L2020, Sigma-Aldrich) and $1x10^5$ hNSCs were seeded in both the right and the left chambers and
780 incubated at 37°C in 5% CO_2 for 24 hours. The medium was then replaced by a neuronal
781 differentiation medium composed of neurobasal medium (10888022, Gibco) supplemented with
782 2% B27 supplement (17504044, Gibco), 1% CultureOne supplement (A3320201, Gibco), 2 mM
783 glutamax (35050038, Gibco), and 200 µM ascorbic acid (A4403, Sigma Aldrich) and incubated at
784 37°C in 5% CO_2 for 14 days, replacing half of the medium every other day. Finally, $2x10^4$ A549-ACE2-
785 TMPRSS2 cells were added over the neurons in both the right and the left chambers in neuronal
786 differentiation medium at 37°C in 5% CO_2 for 48 hours. To assess the SARS-CoV-2 retrograde axonal
787 movement, the right chambers were infected at a MOI of 1 of SARS-CoV-2 Wuhan,
788 Wuhan/ΔORF7ab, Gamma, Delta, or Omicron/BA.1, and incubated at 37°C in 5% CO_2 for 72 hours.
789 To assess the SARS-CoV-2 anterograde axonal movement, the left chambers were infected in the
790 same abovementioned conditions. To prevent passive diffusion of assemblies, hydrostatic pressure
791 was applied by adding medium excess in the reservoirs of recipient chambers [87]. To block the
792 axonal retrograde transport, 100 µM of ciliobrevin D (250401, Calbiochem) was added in the
793 medium during infection and throughout the incubation period. The cells were then fixed with 4%
794 PFA (15444459, Thermo Scientific), washed in PBS, permeabilized with 0.5% Triton X-100 during 10
795 minutes, washed once in PBS, blocked with 10% normal goat serum (10000C, Invitrogen) during 30
796 minutes followed by overnight incubation at 4°C with primary antibodies: mouse anti-β-Tubulin III
797 (neuronal) antibody (1:1000, T8578, Sigma-Aldrich) and rabbit anti-SARS-CoV-2 nucleocapsid
798 antibody (1:1000, GTX135361, GeneTex). The cells were then washed in PBS and incubated with the
799 following secondary antibodies: goat anti-mouse AlexaFluor 647 (1:1000, A21235, Invitrogen) and
800 goat anti-rabbit AlexaFluor 546 (1:1000, A11035, Invitrogen) for 2 hours at 4°C. The cells were then
801 washed, the nuclei were stained with 20 µM Hoechst 33342 (62249, Thermo Scientific) and stored in
802 PBS. Images were obtained using the EVOS FL imaging system (Invitrogen) with the objectives 10x or 20x
803 and the fluorescence cubes DAPI, RFP and CY5.5. Using the same described method, neuron-epithelial
804 networks in microfluidics devices were also infected with the recombinant viruses Wuhan_nLuc,
805 Wuhan/ΔORF7ab_nLuc, and Delta_nLuc at a MOI of 0.5 (maximum volume limitation due to stock viral
806 titer). The nanoluciferase activity in the supernatants was evaluated sequentially at 1, 2 and 3 dpi.
807 Briefly, 20 µL of supernatant was mixed with 20 µL of nLuc substrate (N1110, Promega) in a white 96-
808 wells plate and the luminescence, expressed as Relative light Unit (RLU), was acquired during 100 ms
809 using the VICTOR Nivo Plate reader (Perkin Elmer).
810
811 **Statistics.** Statistical analysis was performed using Prism software (GraphPad, version 9.0.0, San
812 Diego, USA), with $p < 0.05$ considered significant. Quantitative data was compared across groups
813 using Log-rank test, two-tailed Mann-Whitney test or Kruskal-Wallis test followed by the Dunn's

multiple comparisons test. Multivariate statistical analyses on clinical parameters and on tissue inflammation were achieved using Principal Component Analysis. Randomization and blinding were not possible due to pre-defined housing conditions (separated isolators between infected and non-infected animals). *Ex vivo* analyses were blinded (coded samples).

Acknowledgements

The SARS-CoV-2 strain was supplied by the National Reference Centre for Respiratory Viruses hosted by Institut Pasteur (Paris, France) and headed by Pr. Sylvie van der Werf. The human sample from which strain 2019-nCoV/IDF0372/2020 was isolated has been provided by Pr. X. Lescure and Pr. Y. Yazdanpanah from the Bichat Hospital (Paris, France). The human sample from which strain hCoV-19/Japan/TY7-501/2021 (Gamma variant, JPN [P.1]) was supplied by the Japanese National Institute of Infectious Diseases (Tokyo, Japan). The isolate SARS-CoV-2 Delta/2021/I7.2 200 (Delta variant, GISAID ID: EPI_ISL_2029113), the isolate SARS-CoV-2 Omicron/B.1.1.529 (Omicron BA.1 variant, GISAID ID: EPI_ISL_6794907) and the A549-ACE2-TMPRSS2 cells were supplied by the Virus and Immunity Unit hosted by Institut Pasteur and headed by Pr. Olivier Schwartz. We thank Sanjay Vashee from the J. Craig Venter Institute (Rockville, MD, USA) for the YCpBAC-his3 plasmid. This work was supported by Institut Pasteur's Task Force SARS-CoV-2 (NeuroCovid Project), by SARS-CoV-2 joint call Institut Pasteur - Paris Brain Institute (CoVessel Project), by Institut Pasteur's Programme Fédérateur de Recherche 1 (PFR-1 - Reverse Genetics). G.D.M. acknowledges funding from the Fondation pour la Recherche Médicale (grant ANRS MIE202112015304). V.P. is recipient of a fellowship from the European Union's Horizon 2020 Framework Programme for Research and Innovation under Specific Grant Agreement No. 945539 (Human Brain Project SGA3). F.A. is recipient of a fellowship from Institut Pasteur's Programme Fédérateur de Recherche 5 (PFR-5 - Functional Genomics of the Viral Cycle). A.C. acknowledges funding from the Institut Pasteur's 2022-2023 Brain Axis SRA3 M2 Master Student Call. E.S.L and R.K acknowledge support from the Institut Pasteur's Task Force (project SABSOS). E.S.L acknowledges funding from the INCEPTION programme (Investissements d'Avenir grant ANR-16-CONV-0005). We would like to acknowledge Yves Jacob for the fruitful discussions about SARS-CoV-2 ORF7. We thank Etienne Jacotot for his insights on neuronal cultures in microfluidic chambers, as well as Bernadette Bung from MicroBrain Biotech. We also thank Johan Bedel for the help with histopathology, and Emeline Perthame for her insights on statistical analyses. Part of this work was performed at the UtechS Photonic BioImaging (PBI) platform supported by Institut Pasteur and by Région Ile-de-France (program DIM1Health).

Author Contributions

Conceptualization: G.D.M., F.L., and H.B.

Methodology: G.D.M., R.K., V.T., N.R., and F.L.

Investigation: G.D.M., V.P., F.A., A.V.P., S.K., L.K., A.C., M.T., A.P., and A.T.

Funding Acquisition: G.D.M., M.L., P.M.L., N.R., F.L., and H.B.

Resources: B.S.T., D.H., N.W., S.M., R.K., E.S.L., N.R., V.T., and F.L.

Supervision: H.B.

Writing – Original Draft: G.D.M., and H.B.

Writing – Review & Editing: all authors

Conflict of interests

The authors declare no competing interests.

REFERENCES

1. WHO. WHO Coronavirus Disease (COVID-19) Dashboard. https://covid19.who.int/ (2022).
2. Paterson, R.W., *et al.* The emerging spectrum of COVID-19 neurology: clinical, radiological and laboratory findings. *Brain : a journal of neurology* **143**, 3104-3120 (2020).
3. Chou, S.H.-Y., *et al.* Global Incidence of Neurological Manifestations Among Patients Hospitalized With COVID-19—A Report for the GCS-NeuroCOVID Consortium and the ENERGY Consortium. *JAMA Network Open* **4**, e2112131-e2112131 (2021).
4. Klimek, L., *et al.* Olfactory and gustatory disorders in COVID-19. *Allergo Journal International* (2022).
5. Thakur, K.T., *et al.* COVID-19 neuropathology at Columbia University Irving Medical Center/New York Presbyterian Hospital. *Brain : a journal of neurology* **144**, 2696-2708 (2021).
6. Ruz-Caracuel, I., *et al.* Neuropathological findings in fatal COVID-19 and their associated neurological clinical manifestations. *Pathology* (2022).
7. Christensen, P.A., *et al.* Signals of Significantly Increased Vaccine Breakthrough, Decreased Hospitalization Rates, and Less Severe Disease in Patients with Coronavirus Disease 2019 Caused by the Omicron Variant of Severe Acute Respiratory Syndrome Coronavirus 2 in Houston, Texas. *The American Journal of Pathology* **192**, 642-652 (2022).
8. Garrett, N., *et al.* High Rate of Asymptomatic Carriage Associated with Variant Strain Omicron. *medRxiv*, 2021.2012.2020.21268130 (2022).
9. Vihta, K.-D., *et al.* Omicron-associated changes in SARS-CoV-2 symptoms in the United Kingdom. *medRxiv*, 2022.2001.2018.22269082 (2022).
10. Chen, M., *et al.* Evolution of nasal and olfactory infection characteristics of SARS-CoV-2 variants. *bioRxiv*, 2022.2004.2012.487379 (2022).
11. Boscolo-Rizzo, P., *et al.* Coronavirus disease 2019 (COVID-19)–related smell and taste impairment with widespread diffusion of severe acute respiratory syndrome–coronavirus-2 (SARS-CoV-2) Omicron variant. *International Forum of Allergy & Rhinology*, 1-9 (2022).

892 12. Cardoso, C.C., *et al.* Olfactory Dysfunction in Patients With Mild COVID-19 During
893 Gamma, Delta, and Omicron Waves in Rio de Janeiro, Brazil. *JAMA* (2022).
894 13. Butowt, R., Bilińska, K. & von Bartheld, C. Why Does the Omicron Variant Largely
895 Spare Olfactory Function? Implications for the Pathogenesis of Anosmia in
896 Coronavirus Disease 2019 *The Journal of infectious diseases* **226**, 1304-1308 (2022).
897 14. de Melo, G.D., *et al.* COVID-19-related anosmia is associated with viral persistence
898 and inflammation in human olfactory epithelium and brain infection in hamsters.
899 *Science Translational Medicine* **13**, eabf8396 (2021).
900 15. Chan, J.F., *et al.* Simulation of the clinical and pathological manifestations of
901 Coronavirus Disease 2019 (COVID-19) in golden Syrian hamster model: implications
902 for disease pathogenesis and transmissibility. *Clin Infect Dis* (2020).
903 16. Sia, S.F., *et al.* Pathogenesis and transmission of SARS-CoV-2 in golden hamsters.
904 *Nature* **583**, 834-838 (2020).
905 17. Käufer, C., *et al.* Microgliosis and neuronal proteinopathy in brain persist beyond
906 viral clearance in SARS-CoV-2 hamster model. *eBioMedicine* **79**, 103999 (2022).
907 18. Bauer, L., *et al.* Differences in neuroinflammation in the olfactory bulb between
908 D614G, Delta and Omicron BA.1 SARS-CoV-2 variants in the hamster model. *bioRxiv*,
909 2022.2003.2024.485596 (2022).
910 19. Halfmann, P.J., *et al.* SARS-CoV-2 Omicron virus causes attenuated disease in mice
911 and hamsters. *Nature* **603**, 687-692 (2022).
912 20. Mohandas, S., *et al.* Pathogenicity of SARS-CoV-2 Omicron (R346K) variant in Syrian
913 hamsters and its cross-neutralization with different variants of concern.
914 *eBioMedicine* **79**, 103997 (2022).
915 21. McMahan, K., *et al.* Reduced pathogenicity of the SARS-CoV-2 omicron variant in
916 hamsters. *Med* **3**, 262-268.e264 (2022).
917 22. Hayn, M., *et al.* Systematic functional analysis of SARS-CoV-2 proteins uncovers viral
918 innate immune antagonists and remaining vulnerabilities. *Cell reports* **35**, 109126
919 (2021).
920 23. Aliyari, S.R., *et al.* The Evolutionary Dance between Innate Host Antiviral Pathways
921 and SARS-CoV-2. *Pathogens* **11**, 538 (2022).
922 24. Su, C.-M., Wang, L. & Yoo, D. Activation of NF-κB and induction of proinflammatory
923 cytokine expressions mediated by ORF7a protein of SARS-CoV-2. *Sci Rep* **11**, 13464
924 (2021).
925 25. Fogeron, M.-L., *et al.* SARS-CoV-2 ORF7b: is a bat virus protein homologue a major
926 cause of COVID-19 symptoms? *bioRxiv*, 2021.2002.2005.428650 (2021).
927 26. Kim, D.-K., *et al.* A map of binary SARS-CoV-2 protein interactions implicates host
928 immune regulation and ubiquitination. *bioRxiv*, 2021.2003.2015.433877 (2021).
929 27. Mazur-Panasiuk, N., *et al.* Expansion of a SARS-CoV-2 Delta variant with an 872 nt
930 deletion encompassing ORF7a, ORF7b and ORF8, Poland, July to August 2021. *Euro*
931 *Surveill* **26**, 2100902 (2021).
932 28. Panzera, Y., *et al.* A deletion in SARS-CoV-2 ORF7 identified in COVID-19 outbreak in
933 Uruguay. *Transboundary and emerging diseases* **68**, 3075-3082 (2021).
934 29. Jelley, L., *et al.* Genomic epidemiology of Delta SARS-CoV-2 during transition from
935 elimination to suppression in Aotearoa New Zealand. *Nature Commun* **13**, 4035
936 (2022).

30. Pyke, A.T., *et al.* Replication Kinetics of B.1.351 and B.1.1.7 SARS-CoV-2 Variants of Concern Including Assessment of a B.1.1.7 Mutant Carrying a Defective ORF7a Gene. *Viruses* **13**(2021).
31. Renier, N., *et al.* iDISCO: A Simple, Rapid Method to Immunolabel Large Tissue Samples for Volume Imaging. *Cell* **159**, 896-910 (2014).
32. Pepe, A., Pietropaoli, S., Vos, M., Barba-Spaeth, G. & Zurzolo, C. Tunneling nanotubes provide a route for SARS-CoV-2 spreading. *Science Advances* **8**, eabo0171 (2022).
33. Peyrin, J.-M., *et al.* Axon diodes for the reconstruction of oriented neuronal networks in microfluidic chambers. *Lab on a Chip* **11**, 3663-3673 (2011).
34. Sainath, R. & Gallo, G. The dynein inhibitor Ciliobrevin D inhibits the bidirectional transport of organelles along sensory axons and impairs NGF-mediated regulation of growth cones and axon branches. *Dev Neurobiol* **75**, 757-777 (2015).
35. Bauer, L., *et al.* The neuroinvasiveness, neurotropism, and neurovirulence of SARS-CoV-2. *Trends in Neurosciences* **45**, 358-368 (2022).
36. Matschke, J., *et al.* Neuropathology of patients with COVID-19 in Germany: a post-mortem case series. *Lancet Neurol* **19**, 919-929 (2020).
37. Song, E., *et al.* Neuroinvasion of SARS-CoV-2 in human and mouse brainNeuroinvasion of SARS-CoV-2 in humans and mice. *Journal of Experimental Medicine* **218**, e20202135 (2021).
38. Meinhardt, J., *et al.* Olfactory transmucosal SARS-CoV-2 invasion as port of Central Nervous System entry in COVID-19 patients. *Nat Neurosci* **24**, 168-175 (2021).
39. Rutkai, I., *et al.* Neuropathology and virus in brain of SARS-CoV-2 infected non-human primates. *Nature Commun* **13**, 1745 (2022).
40. Ferren, M., *et al.* Hamster organotypic modeling of SARS-CoV-2 lung and brainstem infection. *Nature Commun* **12**, 5809 (2021).
41. Pellegrini, L., *et al.* SARS-CoV-2 Infects the Brain Choroid Plexus and Disrupts the Blood-CSF Barrier in Human Brain Organoids. *Cell Stem Cell* **27**, 951-961.e955 (2020).
42. Ramani, A., *et al.* SARS-CoV-2 targets neurons of 3D human brain organoids. *EMBO J* **39**, e106230 (2020).
43. Kong, W., *et al.* Neuropilin-1 Mediates SARS-CoV-2 Infection of Astrocytes in Brain Organoids, Inducing Inflammation Leading to Dysfunction and Death of Neurons. *mBio* **13**, e0230822 (2022).
44. Khan, M., *et al.* Visualizing in deceased COVID-19 patients how SARS-CoV-2 attacks the respiratory and olfactory mucosae but spares the olfactory bulb. *Cell* (2021).
45. Helms, J., *et al.* Neurologic Features in Severe SARS-CoV-2 Infection. *N Engl J Med* **382**, 2268-2270 (2020).
46. Yang, A.C., *et al.* Dysregulation of brain and choroid plexus cell types in severe COVID-19. *Nature* **595**, 565-571 (2021).
47. Douaud, G., *et al.* SARS-CoV-2 is associated with changes in brain structure in UK Biobank. *Nature* **604**, 697-707 (2022).
48. Abdelnabi, R., *et al.* The omicron (B.1.1.529) SARS-CoV-2 variant of concern does not readily infect Syrian hamsters. *Antiviral Res* **198**, 105253 (2022).
49. Yuan, S., *et al.* Pathogenicity, transmissibility, and fitness of SARS-CoV-2 Omicron in Syrian hamsters. *Science* **0**, eabn8939 (2022).

50. Hui, K.P.Y., *et al.* SARS-CoV-2 Omicron variant replication in human bronchus and lung ex vivo. *Nature* **603**, 715-720 (2022).
51. Armando, F., *et al.* SARS-CoV-2 Omicron variant causes mild pathology in the upper and lower respiratory tract of hamsters. *Nature Commun* **13**, 3519 (2022).
52. Reyna, R.A., *et al.* Recovery of anosmia in hamsters infected with SARS-CoV-2 is correlated with repair of the olfactory epithelium. *Sci Rep* **12**, 628 (2022).
53. Urata, S., *et al.* Regeneration Profiles of Olfactory Epithelium after SARS-CoV-2 Infection in Golden Syrian Hamsters. *ACS Chem Neurosci* **12**, 589-595 (2021).
54. Messlinger, K., Neuhuber, W. & May, A. Activation of the trigeminal system as a likely target of SARS-CoV-2 may contribute to anosmia in COVID-19. *Cephalalgia* **42**, 176-180 (2022).
55. Kishimoto-Urata, M., *et al.* Prolonged and extended impacts of SARS-CoV-2 on the olfactory neurocircuit. *Sci Rep* **12**, 5728 (2022).
56. Zazhytska, M., *et al.* Non-cell-autonomous disruption of nuclear architecture as a potential cause of COVID-19-induced anosmia. *Cell* **185**, 1052-1064.e1012 (2022).
57. Bourgon, C., *et al.* Neutrophils initiate the destruction of the olfactory epithelium during SARS-CoV-2 infection in hamsters. *bioRxiv*, 2022.2003.2015.484439 (2022).
58. Schaecher, S.R., Touchette, E., Schriewer, J., Buller, R.M. & Pekosz, A. Severe Acute Respiratory Syndrome Coronavirus Gene 7 Products Contribute to Virus-Induced Apoptosis. *Journal of Virology* **81**, 11054-11068 (2007).
59. Timilsina, U., Umthong, S., Ivey, E.B., Waxman, B. & Stavrou, S. SARS-CoV-2 ORF7a potently inhibits the antiviral effect of the host factor SERINC5. *Nature Commun* **13**, 2935 (2022).
60. Schaecher, S.R., *et al.* An immunosuppressed Syrian golden hamster model for SARS-CoV infection. *Virology* **380**, 312-321 (2008).
61. Silvas, J.A., *et al.* Contribution of SARS-CoV-2 Accessory Proteins to Viral Pathogenicity in K18 Human ACE2 Transgenic Mice. *Journal of Virology* **95**, e00402-00421 (2021).
62. Imai, M., *et al.* Syrian hamsters as a small animal model for SARS-CoV-2 infection and countermeasure development. *Proc Natl Acad Sci U S A* **117**, 16587-16595 (2020).
63. Bryche, B., *et al.* Massive transient damage of the olfactory epithelium associated with infection of sustentacular cells by SARS-CoV-2 in golden Syrian hamsters. *Brain Behav Immun* **89**, 579-586 (2020).
64. Frere, J.J., *et al.* SARS-CoV-2 infection in hamsters and humans results in lasting and unique systemic perturbations post recovery. *Science Translational Medicine* **0**, eabq3059 (2022).
65. Bulfamante, G., *et al.* Brainstem neuropathology in two cases of COVID-19: SARS-CoV-2 trafficking between brain and lung. *Journal of Neurology* **268**, 4486-4491 (2021).
66. DosSantos, M.F., *et al.* Neuromechanisms of SARS-CoV-2: A Review. *Frontiers in Neuroanatomy* **14**(2020).
67. Ueha, R., *et al.* Oral SARS-CoV-2 Inoculation Causes Nasal Viral Infection Leading to Olfactory Bulb Infection: An Experimental Study. *Frontiers in cellular and infection microbiology* **12**(2022).
68. Dubé, M., *et al.* Axonal Transport Enables Neuron-to-Neuron Propagation of Human Coronavirus OC43. *J Virol* **92**(2018).

1030 69. Shi, J., *et al.* PHEV infection: A promising model of betacoronavirus-associated
1031 neurological and olfactory dysfunction. *PLoS pathogens* **18**, e1010667 (2022).
1032 70. Planas, D., *et al.* Reduced sensitivity of SARS-CoV-2 variant Delta to antibody
1033 neutralization. *Nature* **596**, 276-280 (2021).
1034 71. Zivcec, M., Safronetz, D., Haddock, E., Feldmann, H. & Ebihara, H. Validation of
1035 assays to monitor immune responses in the Syrian golden hamster (Mesocricetus
1036 auratus). *J Immunol Methods* **368**, 24-35 (2011).
1037 72. Gowen, B.B., *et al.* MP-12 virus containing the clone 13 deletion in the NSs gene
1038 prevents lethal disease when administered after Rift Valley fever virus infection in
1039 hamsters. *Front Microbiol* **6**(2015).
1040 73. Espitia, C.M., *et al.* Duplex real-time reverse transcriptase PCR to determine
1041 cytokine mRNA expression in a hamster model of New World cutaneous
1042 leishmaniasis. *BMC Immunology* **11**, 31 (2010).
1043 74. Planas, D., *et al.* Considerable escape of SARS-CoV-2 Omicron to antibody
1044 neutralization. *Nature* **602**, 671-675 (2022).
1045 75. Baer, A. & Kehn-Hall, K. Viral Concentration Determination Through Plaque Assays:
1046 Using Traditional and Novel Overlay Systems. *JoVE*, e52065 (2014).
1047 76. Thi Nhu Thao, T., *et al.* Rapid reconstruction of SARS-CoV-2 using a synthetic
1048 genomics platform. *Nature* **582**, 561-565 (2020).
1049 77. Kouprina, N. & Larionov, V. Transformation-associated recombination (TAR) cloning
1050 for genomics studies and synthetic biology. *Chromosoma* **125**, 621-632 (2016).
1051 78. Kouprina, N., Noskov, V.N. & Larionov, V. Selective isolation of large segments from
1052 individual microbial genomes and environmental DNA samples using
1053 transformation-associated recombination cloning in yeast. *Nature Protocols* **15**,
1054 734-749 (2020).
1055 79. Noskov, V.N., *et al.* A general cloning system to selectively isolate any eukaryotic or
1056 prokaryotic genomic region in yeast. *BMC Genomics* **4**, 16 (2003).
1057 80. Noskov, V.N., Lee, N.C.O., Larionov, V. & Kouprina, N. Rapid generation of long
1058 tandem DNA repeat arrays by homologous recombination in yeast to study their
1059 function in mammalian genomes. *Biological Procedures Online* **13**, 8 (2011).
1060 81. Lindenbach, B.D. Measuring HCV Infectivity Produced in Cell Culture and In Vivo. in
1061 *Hepatitis C: Methods and Protocols* (ed. Tang, H.) 329-336 (Humana Press, Totowa,
1062 NJ, 2009).
1063 82. Lazarini, F., Gabellec, M.-M., Torquet, N. & Lledo, P.-M. Early Activation of Microglia
1064 Triggers Long-Lasting Impairment of Adult Neurogenesis in the Olfactory Bulb. *The*
1065 *Journal of Neuroscience* **32**, 3652-3664 (2012).
1066 83. AVMA. *AVMA Guidelines for the Euthanasia of Animals: 2020 Edition**, (American
1067 Veterinary Medical Association, Schaumburg, IL, 2020).
1068 84. Corman, V.M., *et al.* Detection of 2019 novel coronavirus (2019-nCoV) by real-time
1069 RT-PCR. *Euro Surveill* **25**, 2000045 (2020).
1070 85. Pfaffl, M.W. A new mathematical model for relative quantification in real-time RT-
1071 PCR. *Nucleic Acids Res* **29**, e45-e45 (2001).
1072 86. Renier, N., *et al.* Mapping of Brain Activity by Automated Volume Analysis of
1073 Immediate Early Genes. *Cell* **165**, 1789-1802 (2016).
1074 87. Gribaudo, S., *et al.* Propagation of alpha-Synuclein Strains within Human
1075 Reconstructed Neuronal Network. *Stem Cell Reports* **12**, 230-244 (2019).
1076